A Fixed-scale Pixelated MIMO Visible Light Communication System

A FIXED-SCALE PIXELATED MIMO VISIBLE LIGHT COMMUNICATION SYSTEM

BY

BOXIAO HAN, B.Sc.

A THESIS

SUBMITTED TO THE DEPARTMENT OF ELECTRICAL & COMPUTER ENGINEERING

AND THE SCHOOL OF GRADUATE STUDIES

OF MCMASTER UNIVERSITY

IN PARTIAL FULFILMENT OF THE REQUIREMENTS

FOR THE DEGREE OF

Master of Applied Science

Master of Applied Science (2017) McMaster University

(Electrical & Computer Engineering) Hamilton, Ontario, Canada

TITLE:	A Fixed-scale Pixelated MIMO Visible Light Communication System
AUTHOR:	Boxiao Han B.Sc., (Electronic Information Engineering) University of Electronic Science and Technology of China, Chengdu, China
SUPERVISOR:	Dr. Steve Hranilovic
NUMBER OF PAGES:	xi, 98

To my family

Abstract

Visible light communication (VLC) systems take advantage of ubiquitous light-emitting diodes (LED) and leverage existing illumination infrastructure to provide broadband optical communication links.

Multiple-input multiple-output (MIMO) VLC systems are among the well-studied topics in VLC research. However, most traditional MIMO VLC systems require accurate alignment and have to adjust to different magnifications at various link distances. Consequently, the alignment and calibration modules increase the complexity of the receiver structures.

A pixelated MIMO VLC system is introduced in this thesis, which transmits a series of time-varying coded images that can be received and decoded by commercial digital cameras. Using a convex lens placed in front of the transmitter at its focal length, the system exploits the Bokeh effect to obtain fixed-scale images at all link distances.

Compared with traditional pixelated MIMO VLC systems, which send information directly in space, this spatial-angular mapping system sends information in different angles instead. In contrast to the complex receiver structures in traditional setups, the proposed system can capture fixed-scale images with a simple receiver requiring no re-focusing as the camera moves.

The channel model of the system is measured and modeled and a rateless code is applied to track the truncation of receive images for various link ranges and angular offsets. A proof-of-concept optical communication system is implemented with an LCD display and a high speed CMOS camera. Performance of the system is measured and analysed. The experimental system can achieve a throughput of approximately 10 bit per frame over 90 cm.

This fixed-scale pixelated MIMO wireless optical communication system provides a less expensive option for short-range indoor broadcasting optical links and inter-vehicle communications due to its mobility, stability and simpler receiver structure compared to traditional designs in different working conditions.

Acknowledgements

During my study in the Free-space Optical Algorithms Laboratory of the Department of Electrical and Computer Engineering at McMaster University, I accumulated lots of knowledge and practical experience. Under the supervision of Dr. Steve Hranilovic, I learned a lot about being a decent scholar and a responsible person in life. As my supervisor and mentor in life, he has generously offered me help and advices whenever I am in difficulty and frustrated. I would like to give him my sincere thanks for all the kindness and patience in this journey.

I would also like to give my warmest thanks to all my colleagues in the research group, especially Mr. Min Lu, who helped me set up the experimental system. Mr. George Su also provided me with a lot of advices on the coding part. Mr. Warren Pawlikowski shared his experience in the hardware area and he has always been a reliable helping hand when I encountered any hardware problem. It is indeed a great honour to work in a group with such diversity and talents.

Lastly, I would like to thank my parents for all their love in all these years. They are always my strongest support no matter where I am and how well I am doing.

Again, thanks to everyone for all your help.

Contents

Abstract **iv**

Acknowledgements **vi**

1 Introduction **1**

1.1 Wireless Optical Communications 1

1.2 MIMO Optical Wireless Systems 6

1.2.1 Two-dimensional Barcodes 6

1.2.2 Holographic Storage System 8

1.2.3 Non-pixelated MIMO VLC Systems 9

1.2.4 Pixelated MIMO VLC Systems 10

1.3 Contributions of this Thesis 13

1.4 Thesis Structure 15

2 Fixed-scale MIMO Channel Modeling **16**

2.1 Overview 16

2.2 Generalized Channel Model 20

2.2.1 Coordinate Systems 20

2.2.2 Mapping between Coordinate Systems 22

2.3 Windowing Effect 23
2.3.1 Window Diameter 24
2.3.2 Window Center 27
2.3.3 Special Case 28
2.3.4 Window Gain 30
2.4 Point Spread Function and Noise 33
2.4.1 Point Spread Function 33
2.4.2 Noise 34
2.5 Communication Model 35
2.5.1 Overall Model 35
2.5.2 Tradeoffs 38
2.6 Summary 39

3 System Design **40**
3.1 System Design and Parameter Selection 41
3.1.1 Transmitter Selection 41
3.1.2 Receiver Selection 43
3.1.3 Lens Selection 44
3.2 Design Examples 47
3.3 Raptor Codes 48
3.4 Localization Benefits 52
3.5 Conclusion 54

4 Experimental System and Measurement Results **55**
4.1 Experimental Setup and Parameters 56

4.2 Channel Measurements 57
4.2.1 Magnification 58
4.2.2 Truncation Window 60
4.3 Rate Measurements 64
4.3.1 Information Rate 64
4.3.2 Throughput 66
4.4 Comparison to Conventional MIMO Pixelated System 67
4.5 Conclusion 69

5 Conclusions and Future Directions **70**
5.1 Future Work 72

A Calculation of Window Diameter **74**

B Calculation of Window Center **77**

C Computation of Window Gain **80**

List of Figures

1.1 Different Types of 2D Barcodes (Generated from [1] with Information: Pixelated MIMO Visible Light Communication System) 8

1.2 A Pixelated MIMO VLC Channel Configuration 11

2.1 Calculation of Magnification in Fixed-scale Pixelated MIMO Channel 18

2.2 Calculation of Magnification in Traditional Pixelated MIMO Channel 20

2.3 General Fixed-scale MIMO VLC System Architecture 21

2.4 Relation between RCS and TCS 22

2.5 Parameters of the Truncation Window in Pixelated MIMO Channel . 24

2.6 Calculation of Window Parameters (General Case) 25

2.7 Calculation of Window Parameters (Special Case) 29

2.8 Calculation Process of the Window Gain 30

2.9 Simulation of one example of Normalized Gain Function, only values along the diameter $x = 0, y \in [-0.5, 0.5]$ is plotted. 32

2.10 The Block Diagram for Fixed-scale MIMO VLC System 36

3.1 Numerical Aperture 46

3.2 Demonstration of the Raptor Code Encoder Structure (figure based on Fig. 1 in [2]) 50

3.3 Mapping of Raptor 10 packets to the transmit image for fixed-scale MIMO system. Notice that systematic packets (highlighted packets) are placed near the optical axis under the assumption that orientation will be typically satisfied. 51
3.4 Localization Benefits 52
4.1 Experimental Setup of the Fixed-scale Pixelated MIMO System . . . 56
4.2 Magnification under Different Translations 58
4.3 Window Diameter in Different Situations 60
4.4 Comparison of Different Distances and Translations 62
4.5 Comparison of Window Gains 63
4.6 Information Rate 65
4.7 Data rates. The red solid curve indicates the maximum information rate subject to binary modulation of each transmit sub-channel over u. Realized data rates with Raptor 10 codes for $|\vec{\delta}| = 0, 3$ mm are also plotted. 66
A.1 Calculation of Window Parameters with Temporary Coordinates . . . 75
C.2 Detailed Calculation Process of Window Gain 81
C.3 Calculation of Window Gain (Case I) 82
C.4 Calculation of Window Gain (Case II) 83
C.5 Calculation of Window Gain (Case III) 84
C.6 Calculation of Window Gain (Case IV) 85
C.7 Relation Between $|y|$ and $|O_tO_r|$ 85

Chapter 1

Introduction

1.1 Wireless Optical Communications

In the past decade, the rapid growth of the smart device industry and the ubiquitous mobile Internet have caused an ever increasing demand for mobile data exchanges. The emerging concept of Internet of Things (IoT) even further boosts the need of reliable high-speed wireless networks. According to [3], the global mobile data traffic has grown over 60% in 2016 alone.

The current wireless network markets are primarily dominated by radio frequency (RF) technologies, of which the frequency spectrum is strictly regulated between 30 kHz to 300 GHz [4]. Licensed by different authorities, the limited RF spectrum is facing the problem of spectrum congestion [4]. As an alternative (or complementary) solution, optical wireless communications (OWC) have received growing attention from academia and industries with relatively unexplored potentials. Compared to RF technologies, OWC enjoy a range of advantages such as license-free frequency spectrum, inherent security, broader bandwidths and

bandwidth reuse potential with good spatial confinements [4, 5]. OWC systems are mostly based on the following three optical bands: infrared light (IR), ultraviolet light (UV) and visible light spectrum.

One typical example of OWC systems is the free space optical (FSO) systems. Mostly implemented with lasers, many of the FSO systems operate at the near-IR frequencies (800 nm to 1550 nm) [4]. FSO systems are often used for deep-space communication and terrestrial point-to-point data transmission over longer ranges (on the order of kilometers). When transmitting modulated laser beams, the FSO links are easily affected by weather conditions. Impacts of these different factors were studied in [6, 7] and the performance of the links was shown to be more easily impaired by fogs compared to other weather conditions because of the operating wavelength of the systems [8]. Different advanced technologies such as multiple-input multiple-output (MIMO), adaptive transmission and RF/FSO hybrid systems were also introduced into FSO systems according to [9–12]. In a recent paper [13], an experimental FSO system using wavelength multiplexing was implemented and a data rate of 1.6 Tbps was achieved.

Systems based on UV frequencies have also been intensely studied in recent years. In deep-UV band (200 nm to 280 nm) [4], due to the progress in UV sources and solar-blind detector technologies, various non-line-of-sight (NLOS) communication links with low cost and higher energy efficiencies were implemented and analysed. In [14], a communication system based on UV light was built over ranges less than 1 km with a bit error rate of 10^{-3}.

Visible light communication (VLC) is also gaining increasing attention from researchers thanks to the rapid development of the solid-state lighting technology.

Especially, the progress in white light-emitting diode (WLED) technology provides a promising future for an LED-dominated illumination industry [15]. According to [16], LED lighting is predicted to increase its market share to 84 % by 2030. Compared to traditional incandescent bulbs and fluorescent lamps, LEDs have several superior features such as longer lifespan (60 kilohours compared to 10 kilohours), higher power efficiency (over 50% more efficient) and less environmental impacts (mercury-free) [17–20].

As a subset of OWC, VLC not only enjoys the same advantages as OWC, but also possesses its unique attractive features. VLC can leverage existing light-emitting diode (LED) illumination infrastructure to provide broadband optical communication links [21]. Transmitters are ubiquitous and found in LED lighting, backlighting and display technologies among many others. Equally ubiquitous mobile devices with integrated cameras offer great potential to work as VLC receivers. Therefore, VLC links can be potentially combined with other existing applications to provide lighting, traffic signalling along with intense data exchanges. Pioneered by Visible Light Communication Consortium (VLCC), VLC technology has made great progress towards the standardization. In 2012, the first standard of VLC [22] was published and on-off keying (OOK) , color shift keying (CSK) and variable pulse position modulation (VPPM) were recognized as modulation schemes. Data rate up to 96 Mb/s is supported in [22]. Based on IEEE 802.11, light-fidelity (LiFi) employs orthogonal frequency-division multiplexing (OFDM) to implement a complete wireless network system and is considered to be added to the coming standard of VLC systems [23, 24]. Commercial companies such as PureLiFi [25] and ByteLight [26] have also contributed to the development and standardization of

VLC. The most recent product of PureLiFi is named LiFi-X and can achieve a data exchange rate of 40 Mbps [27].

Though LED illumination devices are widespread, they are typically not optimized for communication applications and have limited modulation bandwidth between 2-20 MHz [28]. Most white LEDs in illumination markets are based on two mainstream technologies. One is the phosphor-based LED, which combines a blue LED with a yellow phosphor coating. The phosphor can emit yellow light by absorbing part of the blue photons to produce white light to human eyes. When the phosphor coating absorbs the blue light and produces yellow light, a decay time of around 100 ns limits the modulation bandwidth of the LED to around 2 MHz [29]. The other is the red-green-blue (RGB) LED that produces white light by mixing red, green and blue light. Without a phosphor coating, the RGB LED has a higher bandwidth potentially (up to 100 MHz) compared to the phosphor-based LED [28]. However, due to its simpler structure and low cost, the phosphor-based LED is often used for communication purpose.

To increase the bandwidth efficiency, different methods can be applied [20]. By adding an optical filter at the receiver to remove the unmodulated yellow light of a system using phosphor-based LED, the bandwidth of the system can be increased to about 12 MHz [30]. In addition to increasing the modulation bandwidth of the system, bandwidth efficient modulation schemes, such as pulse amplitude modulation (PAM), variable pulse position modulation (VPPM) and color shift keying (CSK) for RGB LEDs, can be used to increase the data throughput with high signal to noise ratio (SNR) (over 60 dB) [22, 30].

Inspired by RF communications, multi-carrier techniques were also introduced to

VLC systems by researchers to obtain superior performance. OFDM can utilize the available bandwidth efficiently by assigning data adaptively to different frequency bands [31]. Different from RF links, optical OFDM systems are based on intensity modulation/direct detection (IM/DD) model, which means the transmitted OFDM signals have to be strictly positive. One approach to satisfy non-negativity is to introduce a direct current (DC) bias, known as DC-biased optical OFDM (DCO-OFDM). However, such scheme increases the power dissipation and if the DC bias is not excessively large, part of the negative signals need to be clipped, thus introducing clipping noise to the system [32]. Asymmetrically-clipped optical OFDM (ACO-OFDM) was proposed where only half of the sub-carriers are modulated [33] and the bipolar signal is then clipped at zero level. Modulating only the odd sub-carriers of the signal, the clipping will not impair the data-carrying sub-carriers while ensuring non-negativity. A more detailed comparison of these two techniques were provided in [34] using quadrature amplitude modulation (QAM). Except for large constellation size such as 1024-QAM, ACO-OFDM was shown to require less optical power compared to DCO-OFDM with a fixed data rate and bit error rate according to [34]. Combination and variation of these two OFDM schemes were also introduced in [35, 36] for better performances in various conditions. In a similar direction, symmetrical clipping and discrete multitones (DMT) were employed to achieve a data rate up to 500 Mb/s in [37].

Analogous to RF communications, MIMO technology has also been extensively investigated in VLC systems in order to improve link speed or stability.

1.2 MIMO Optical Wireless Systems

First introduced in RF communications in the late 1980s, a MIMO system consists of multiple numbers of transmit and receive antennas compared to traditional single-input single-output systems. MIMO technology is widely used in RF systems to increase spectral efficiency and link reliability. RF wireless communication standards including IEEE 802.11n, IEEE 802.11ac, HSPA+ and Long Term Evolution (LTE) all employ MIMO as a crucial element [38]. Inspired by this technique, various MIMO optical wireless systems are also constructed. With smaller operating wavelength compared to RF links, MIMO optical wireless systems are often constructed with a large number of transmit and receive elements as described in [5, 39]. Moreover, in MIMO optical systems, the area of the sensor arrays are usually on the order of millions of square wavelengths. According to [40], when the optical intensity field is integrated over the sensor arrays to form the receive images, an inherent spatial diversity can be achieved in such systems.

In this section, a brief review of various types of MIMO optical wireless systems and approaches is presented. Drawbacks of the existing systems will also be discussed to provide our newly proposed system with a solid background.

1.2.1 Two-dimensional Barcodes

The simplest forms of MIMO optical wireless systems are two-dimensional (2D) barcodes. As an optical, machine-readable spatial representation of data, 2D barcodes are widely applied in commercial transportation, bank management and postal industry. Most 2D barcodes encode data in an array of printed pixels that can be imaged with a camera or a scanner. This is analogous to a one-frame

pixelated MIMO VLC system with the barcode acting as one single frame of 2D transmit image.

Among different types of 2D barcodes, the most popular ones are quick response codes (QR Codes) [41]. Take QR codes for example, black squares are arranged on a white background to represent the encoded information. Required patterns at the corners of the barcodes can provide the receiver with position information. Alignment and timing information can also be included in some versions of QR codes. To achieve reliable data transmission, Reed-Solomon error correction is applied to ensure correct decoding operations. Other types of 2D barcodes, such as Data Matrix Codes [42] and Aztec Codes [43], are slightly different in the way data is encoded and arranged. However, most 2D barcodes require certain finder patterns in the codes to help the receiver correctly locate the barcodes. Constraints on imaging distance and alignments are also comparatively strict in order to obtain data from a single image correctly. In Fig. 1.1, three types of 2D barcodes are depicted and each barcode includes finder patterns.

A novel type of 2D barcode, "Bokode" was presented in [44]. Different from traditional 2D barcodes, a collimating lens was introduced in front of the Bokode pattern. This lens can be thought of as performing a space-to-angle mapping and all data are thus transmitted in the angular domain rather than in space directly. A camera receiver is required to focus at infinity to form a fixed-scale image on the sensor utilizing the "Bokeh" effect. In [44], an experimental Bokode was implemented with a single lenslet and an off-the-shelf camera. Bokode of size 2.5 μm was successfully captured over 4 m. Two major advantages of Bokode are fixed-scale receive images at all working distances and no need to re-focus the

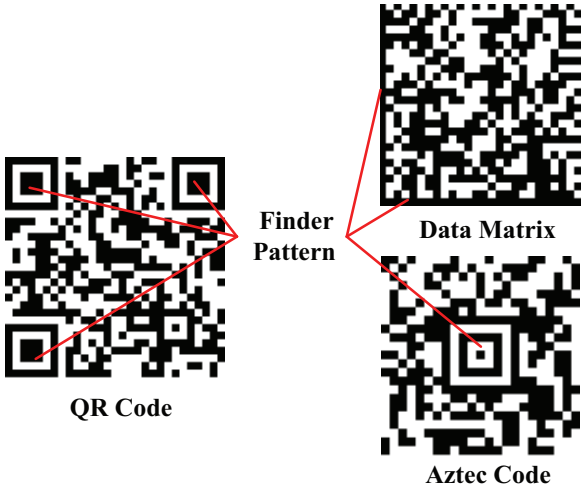

Figure 1.1: Different Types of 2D Barcodes (Generated from [1] with Information: Pixelated MIMO Visible Light Communication System)

camera as it moves. As a tradeoff, due to the limited angular subtense of the camera lens, the receive images are truncated by a window of which the size is dependent on different separation distances between the transmitter and receiver.

1.2.2 Holographic Storage System

As a high-capacity data storage technology, holographic storage system can be considered as a special variation of MIMO optical wireless communication systems. Different from most MIMO optical wireless communication systems, which are incoherent and based on IM/DD channel model, the holographic storage systems use coherent light to enable recording and reading data [45].

A typical holographic storage system multiplexes and modulates data spatially into 2D coherent images. Signal beams are then created by projecting the coherent images into series of lenses. Intersecting with the signal beams, reference beams are applied to form interference patterns, which are then superimposed in the thick

photosensitive materials. To read the data from a certain frame, the corresponding reference beam (readout beam) is employed to reconstruct the coherent image. A detector array is then used to recover the original data [45, 46]. Compared with traditional magnetic storage mediums that record data only on the surface of the materials, holographic storage systems store data throughout the volume of the materials and are vulnerable to optical distortions (blurs) as well as errors in magnification [47]. In 2006, InPhase Technology published a white paper of a holographic data storage system achieving experimental data densities of 500 Gbit/in^2 with a write user rate of 23 MB/s and a read rate of 13 MB/s [48].

1.2.3 Non-pixelated MIMO VLC Systems

Similar to RF MIMO systems, there is a well-established body of research on MIMO VLC systems with small number of transmit and receive elements.

In [49], a MIMO setup with 2×2 transmitter array and 2×2 receiver array was presented with spatial multiplexing. OOK was used in each transmitter. Both imaging and non-imaging receivers were compared. It was shown that due to spatial symmetry of element arrays, the non-imaging receiver did not operate properly in some cases while the imaging receiver was shown to be robust at different positions. Both designs achieved data rates of several hundred Mbit/s and misalignment such as rotation was shown to affect the system design process.

A multi-Gigabit/s indoor VLC system was also presented in [50] using MIMO-OFDM and a 2×2 channel setup. In each channel, software based OFDM signals were transmitted and a 3×3 receiver array was used. At 1 m distance, a data rate of 1.1 Gb/s was achieved and an average bit error rate of 10^{-3} was observed at room

illumination. However, this setup required strict focus operation at a fixed distance, thus limiting the mobility of the system.

In [51], MIMO wireless optical system employing a new modulation scheme, termed optical spatial modulation (OSM), was presented. The basic idea of OSM is to use the spatially separated transmitters as spatial constellation points. In each time interval, only one of the multiple transmitters is activated to send optical signals. The active transmitter is determined by the input data sequence and a photodiode-based receiver is used to recover the active transmitter index by its unique propagation condition [52]. In [51], an indoor simulation system based on 2×2 transmitters was built and the bit error rate was examined under different alignment conditions and with different receiver arrays. It was shown that increasing the number of receivers can enhance the system performance by increasing the rank of the channel matrix. By carefully aligning the transmitter and the receiver, the channel matrix was shown to be nearly diagonal, thus de-correlating the propagation path of each individual transmitter. With only one active transmitter, the OSM system can avoid inter-channel interference and allow for a simpler receiver structure. Since multiplexing is achieved by single optical source, the system power consumption can also be reduced [51]. However, the system performance was shown to be greatly impacted by the alignment between the transmitter and the receiver according to [51].

1.2.4 Pixelated MIMO VLC Systems

As mentioned in Section 1.1, due to the shorter wavelength of visible light, a MIMO VLC system is often implemented with large number of transmit and receive

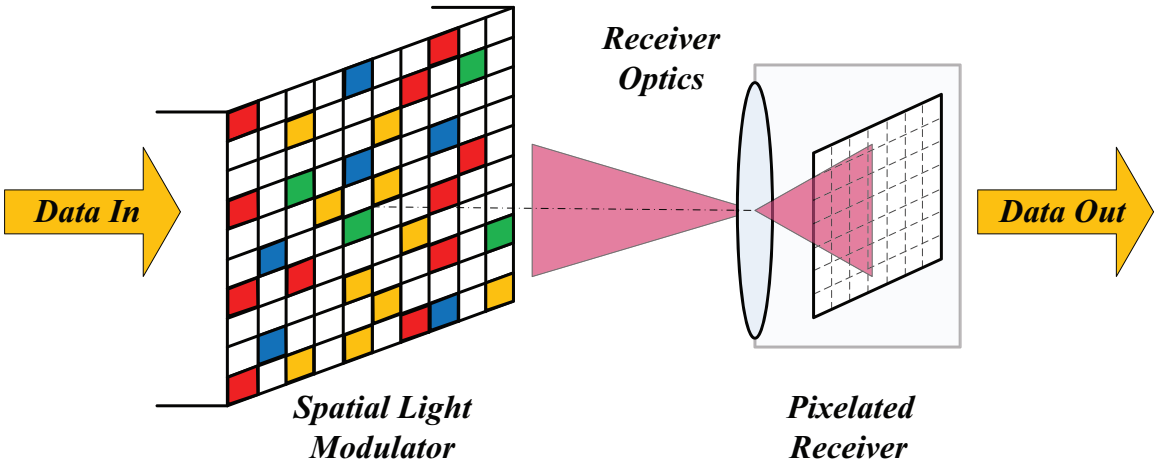

Figure 1.2: A Pixelated MIMO VLC Channel Configuration

antennas (elements). Each transmit or receive element can be viewed as a pixel in this case and such system can be termed "pixelated". Since a pixelated MIMO VLC system is equivalent to a system that transmits and receives visible images, it is also known as visual MIMO systems [53, 54]. As extensions of the one-frame 2D barcodes, pixelated MIMO VLC systems are investigated by researchers to realize real-time data transmission.

Similar to [45], a typical configuration of pixelated MIMO VLC channel is presented in Fig. 1.2. The transmitter is an array of optical intensity emitters that can be independently addressed and modulated in time. Such transmitter can be termed a spatial light modulator (SLM), which generates intensity images by electrically addressing each pixel. The receiver is an imaging device based on an array of detectors. The input data is firstly multiplexed and modulated in space to form an intensity image for transmission. The receiver then captures and reconstructs the transmitted image on the sensor array. Original data can be retrieved from this image as output.

In [40], a short-range pixelated MIMO VLC system was demonstrated. A liquid-crystal display (LCD) was used to send a series of coded images that were captured by a high speed camera. Spatial discrete multitone (SDMT) was applied to achieve spatial multiplexing gain without the need of precise spatial alignment and capacity of the channel was calculated with water-filling algorithm. However, channel knowledge is required to adjust the magnification to avoid aliasing. Moreover, the proposed system was implemented with a fixed distance of 2 m between the transmitter and the receiver, thus limiting the mobility of related applications.

Similar work was also presented in [55]. The impact of vignetting on SDMT (called spatial OFDM in the paper) was explored and vignetting was shown to cause attenuation as well as inter-carrier interference (ICI) spatially. The use of spatial asymmetrically clipped optical OFDM and spatial DC-biased OFDM were also compared. The former scheme was found to be more robust to vignetting than the latter one.

Pixelated MIMO VLC systems based on 2D barcodes were also presented in [53, 54, 56–58]. For instance, in [53], LCD-to-tablet (integrated camera) systems were built. Multiplexing and diversity gains were characterized in the presence of perspective distortions, different viewing angles and blurs. The capacity of such system was shown to be greatly impacted by perspective distortions. A switch between multiplexing and diversity modes of the system was found to be dependent on separation distances of the LCD and the tablet. When the distance is small (multiplexing mode), each of the transmit pixel (sub-channel) can be captured by several receive pixels, thus realizing multiple parallel sub-channels. When the distance grows large, due to the change of magnification, signals from different

transmit pixels are projected onto one or a few pixels. Therefore, the system is considered to be in the diversity mode where the same signals can be sent from different transmit pixels to enhance the reliability of the system. The experimental system was based on 2D barcodes in each frame and required calibration steps to obtain parameters such as magnification and focal distance.

Rate adaption in pixelated MIMO VLC system was also explored. In [59], a rate adaptive scheme named visual MIMO rate adaptation (VMRA) was implemented and tested for inter-vehicle communication. The basic idea of VMRA was to adjust the transmission rate by switching between different spatial transmission patterns based on different packet error feedbacks from the receiver. In a similar direction, [57] also proposed a rate adaptive scheme by changing the size of the transmitted images. Analogous to [53], these rate adaption systems required complex tracing algorithms based on computer vision to track distances between the transmitter and the receiver.

One common thread in these previous studies is that MIMO VLC systems were sensitive to a variety of impairments and careful calibration was required to compensate for misalignment, defocus aberration, magnification, vignetting and receiver orientations [30]. Most of these drawbacks can be alleviated by designing more complex receivers and calibration algorithms. However, considering optical links are often used for data transmission to multiple users, such solutions are not ideal for practical use.

1.3 Contributions of this Thesis

The work in this thesis is summarized in the paper submitted in [60]. To cope with various problems associated with traditional MIMO VLC systems, a fixed-scale

pixelated MIMO VLC system is proposed. There are three major contributions made in this thesis:

(1) Introducing the novel idea of the fixed-scale pixelated MIMO VLC system: The 2D Bokode in Chapter 1 is extended into a multiframe MIMO VLC system. Benefiting from the extra collimating lens, fixed-scale images can be captured at different positions and orientations with the camera focusing at infinity. Compared to traditional systems proposed in [40, 53, 55], this newly presented system simplifies the receiver structure and alleviates the impairments due to misalignment while ensuring good mobility.

(2) Presenting models and design guidelines for the fixed-scale pixelated MIMO VLC system: Although basic analyses were available in [44], no theoretical description was provided for cases where translation and tilting of the receiver occurred. In Chapter 2, a detailed channel model including translation, tilting and truncation effect is constructed.

A mathematical communication model for the proposed system is also built to set up a theoretical framework for system design. Based on this communication model, design guidelines on how to achieve a higher data rate are provided in Chapter 3. Parameter and component selection is also discussed by balancing between cost and performance. A designer can obtain both theoretical and practical understanding of the fixed-scale pixelated MIMO VLC system by reading this thesis.

(3) Combining the fixed-scale pixelated MIMO VLC system with rate-adaptive Raptor codes: With different truncations at different separation distances, pixelated MIMO VLC system possesses an inherent need of rate adaption. A Raptor 10 code [61] is employed in this system to achieve reliable data transmission while ensuring

efficient channel utilization. Combined with a Raptor code, the proposed system is able to track different sub-channel numbers due to truncation and automatically adjust the data rate. Such systems can serve as an underlying option for indoor short-range data networks.

1.4 Thesis Structure

The thesis is organized as follows. Chapter 2 discusses the basic features of the fixed-scale pixelated MIMO channel and presents a general channel model. The truncation effect is also examined and an overall communication model is constructed. Based on the theory in Chapter 2, Chapter 3 introduces the system design process as well as the application of Raptor 10 code. In Chapter 4, a proof-of-concept system is designed and simulation as well as experimental data are presented. Finally, in Chapter 5, general conclusions are drawn and future directions are given.

Chapter 2

Fixed-scale MIMO Channel Modeling

In this chapter, a detailed channel model of the fixed-scale pixelated MIMO optical system is firstly presented. Based on ray optics, analyses are provided on how the inherent spatial-angular mapping helps the system achieve a fixed magnification. The model is then shown to be robust to different receiver translations and orientations. As a unique feature of the fixed-scale pixelated MIMO optical channel, the truncation effect is also modeled and parameterized. Using this truncation model, an end-to-end communication model can be constructed to estimate the performance of the proposed system in regard to different parameters.

2.1 Overview

Fig. 2.1 presents a block diagram of the fixed-scale pixelated MIMO VLC channel. The transmitter is an array of optical intensity emitters, termed *transmit pixels*, which

can be independently addressed and modulated in time. A convex collimating lens, termed *transmit lens*, of focal length f_1 is placed in front of the transmitter array. After a propagating distance of u, a receiver camera, focused at infinity, is deployed to capture the receive image. The camera lens in the receiver is termed *receive lens* and the pixels of the camera sensor array are termed *receive pixels*.

This optical configuration, firstly proposed in [44], maps each transmit pixel position to a set of transmitted angles relative to the normal of the transmit lens. That is, the transmit lens can be thought of as performing a space-to-angle mapping of the transmitted data whilst the receiver lens performs this inverse operation.

Inspired by microscopes, such configuration is analogous to the infinity corrected microscope. The transmit lens can be considered as "objective" of the microscope and the receive lens acts as the "eyepiece" [44].

Compared to an infinity corrected microscope, there is no tube connecting both lenses in this new configuration. As a drawback, the performance of this system may be more easily impaired by different background illumination conditions between the two lenses [44]. However, this design enables the potential of multiple receivers operating simultaneously. Such feature is attractive especially for indoor optical broadcasting applications.

Similar to the microscope, the magnification of the receive image is determined by both transmit and receive lenses in this system. As discussed in Section 3.1, by selecting the proper lenses, fixed-scale receive images can be captured by the camera regardless of the distance between two ends. The magnification can be derived based on ray optics as follows.

Consider the system diagram in Fig. 2.1 where f_1 and f_2 are the focal lengths of

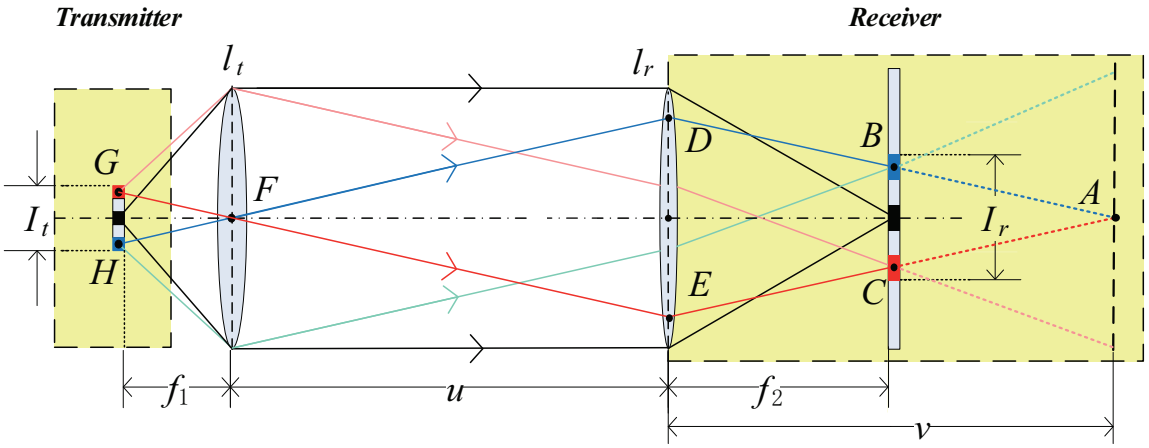

Figure 2.1: Calculation of Magnification in Fixed-scale Pixelated MIMO Channel

the transmit and receive lens respectively separated by distance u (measured between optical centres of the lenses) and I_t, I_r are the sizes of the transmit image and the corresponding receive image. The magnification, M, of the optical system is defined as:

$$M = \frac{I_r}{I_t}. \tag{2.1}$$

Assume the transmit image is comparatively small in size so that most rays emitted from the transmit image can satisfy the paraxial approximation [62]. Under such assumption, thin lens formula is applied to obtain:

$$\frac{1}{f_2} = \frac{1}{u} + \frac{1}{v}. \tag{2.2}$$

Notice there are two pairs of similar triangles: $\triangle ABC \sim \triangle ADE$ and $\triangle FGH \sim \triangle FED$, their relation can be written as:

$$\begin{aligned} \frac{|DE|}{I_r} &= \frac{v}{v - f_2} \\ \frac{|DE|}{I_t} &= \frac{u}{f_1}. \end{aligned} \tag{2.3}$$

Simply combining (2.2) with (2.3) yields the magnification of the system:

$$M = \frac{f_2}{f_1}. \tag{2.4}$$

Notice that M is independent of the distance u while in conventional pixelated MIMO optical wireless systems as shown in Fig. 2.2, the magnification $M \propto 1/u$. Hence, in this *fixed-scale* pixelated MIMO system, the scale of each transmit pixel captured at the camera stays fixed while removing the need for re-focusing when the receiver location changes. Alternatively, the transmitter sends data in angular domain rather than directly in spatial domain. As u increases, the set of angles subtended by the receiver is reduced, resulting in a truncation of transmit pixels visible to the receiver.

This significant feature simplifies the design of the receiver because with fixed-scale receive images at all distances, the camera no longer has to estimate different magnifications as those in traditional configurations. Moreover, without the need to re-focus the camera, no strict alignment is required when the receiver moves. Such advantages will be exploited to design a wireless optical communication system with multiple potential mobile users and simple receiver structures in Chapter 4.

In the following, a detailed model of this optical communications channel is presented.

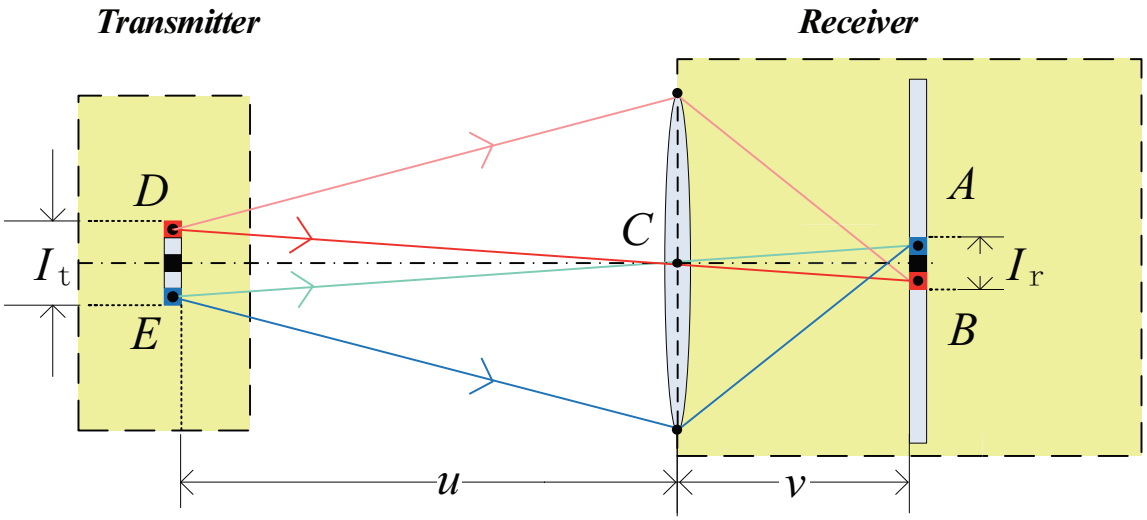

Figure 2.2: Calculation of Magnification in Traditional Pixelated MIMO Channel

2.2 Generalized Channel Model

In practice, the transmitter and receiver may not be perfectly aligned as shown in Fig. 2.3, considering the position and orientation of the receiver. A generalized model of such case is presented. In order to describe this situation more efficiently, two coordinate systems are firstly introduced.

2.2.1 Coordinate Systems

Fig. 2.3 shows a cross-sectional view of the system in the plane formed by the optical axes of both lenses. Define the *transmit coordinate system* (TCS) in Fig. 2.3 centered at O', which is the intersection point of the transmit image plane and the optical axis of transmit lens, denoted by (x', y', z'). Analogously, define the *receive coordinate system* (RCS) centered at O, which is the intersection of the receive image plane and the optical axis of receive lens, with coordinates denoted by (x, y, z).

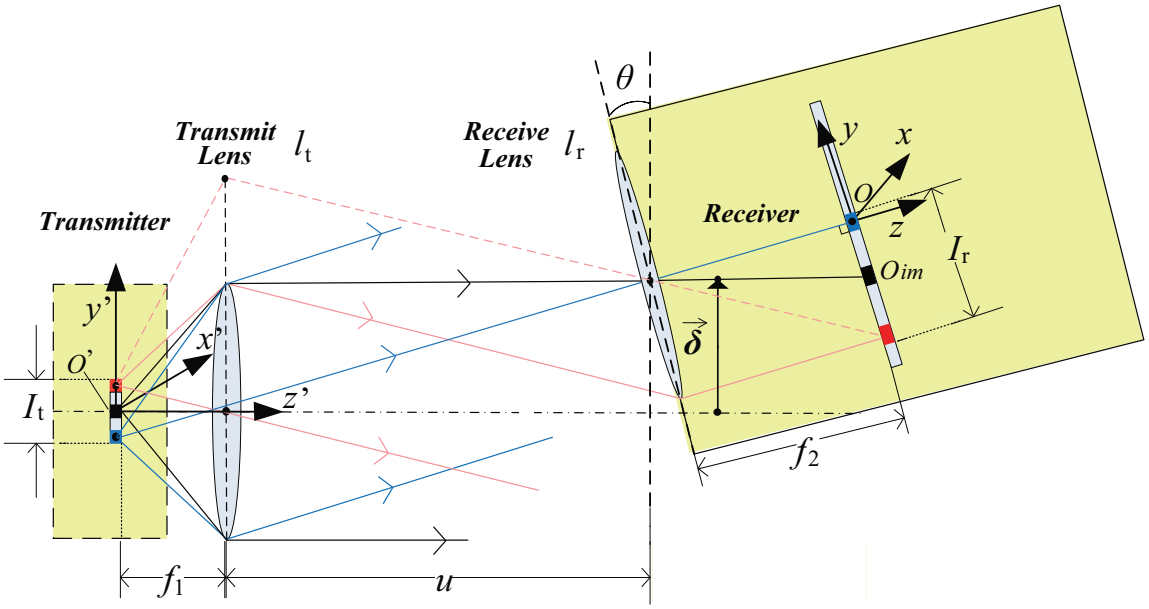

Figure 2.3: General Fixed-scale MIMO VLC System Architecture

The z-axes of both coordinate systems are defined along the optical axes of each lens respectively as Fig. 2.3 shows. The axes of the two coordinate systems are adjusted so that the two y-axes lie in the same plane as the optical axes of both lenses. Following the right-handed coordinate rule, x-axes can be determined. In Fig. 2.3, z-axes and y-axes are shown to lie in the same plane formed by the two optical axes. The two x-axes are co-linear as the figure indicates.

The transmitter and receiver are separated over a range u measured as the distance between the optical centers of the lenses along the optical axis of transmit lens. In general, the optical center of the receive lens is displaced by a vector $\vec{\delta}$ pointing from the optical axis of transmit lens to the optical center of the receive lens along the normal direction. Additionally, as shown in the figure, the axes can also be inclined relative to each other. As a simplifying assumption, we assume that the RCS is rotated by θ about the x-axis towards the transmitter.

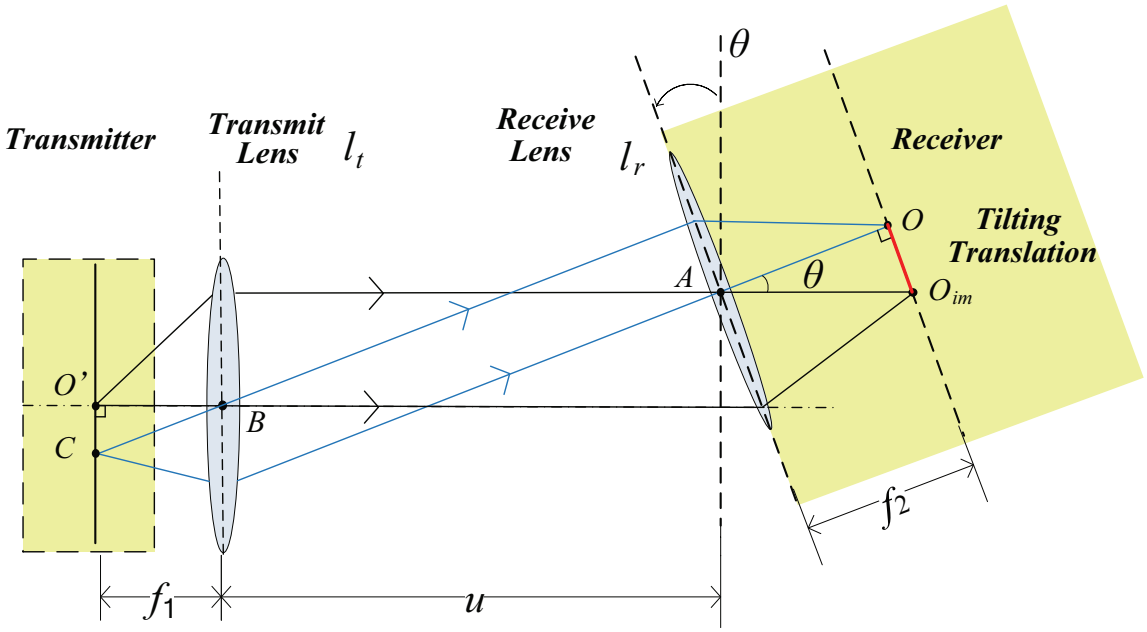

Figure 2.4: Relation between RCS and TCS

2.2.2 Mapping between Coordinate Systems

Based on the two coordinate systems defined in the Section 2.2.1, the mapping between TCS and RCS is discussed. In the general case, the magnification and image position are firstly investigated to ensure this fixed-scale model still holds.

In the case where $\theta = 0$, it can be easily shown the origin O' in TCS maps to O in RCS regardless of $\vec{\delta}$ or u. This can be justified by noting that the angle of each transmitted ray relative to the normal of the receive lens is unaffected by changing range, u, or shift, $\vec{\delta}$.

In the general case, if the optical axes of transmit and receive lenses are tilted by angle θ, where $\theta \in [0, \pi/2)$, O' maps to O_{im} and point C maps to O in RCS instead. As Fig. 2.4 indicates, similar triangle pair $\triangle AOO_{im} \sim \triangle BO'C$ is formed. Use $|AO|$ to denote the length of segment AO, their relation is written as:

$$\frac{|AO|}{|BO'|} = \frac{|OO_{im}|}{|O'C|} \tag{2.5}$$

where $|AO| = f_2$ and $|BO'| = f_1$. According to (2.4), the magnification in this case can be determined as $M = \frac{|OO_{im}|}{|O'C|} = \frac{f_2}{f_1}$.

Although the magnification M is shown to stay fixed as predicted, there is still a fixed translation between the TCS and RCS, termed *tilting translation*, t. This translation occurs because the angle of each transmitted ray relative to the normal of the receive lens is modified by the tilt of the receiver. As shown in Fig. 2.4, the translation can be calculated in the right triangle $\triangle AOO_{im}$ as $t = |OO_{im}| = f_2 \tan\theta$. Notice, however, that the translation between TCS and RCS remains independent of $\vec{\delta}$, u.

Based on previous analyses, the mapping between TCS and RCS can be compactly written as:

$$\begin{bmatrix} x \\ y \\ z \end{bmatrix} = \begin{bmatrix} -M & 0 & 0 \\ 0 & -M & 0 \\ 0 & 0 & 0 \end{bmatrix} \begin{bmatrix} x' \\ y' \\ z' \end{bmatrix} + \begin{bmatrix} 0 \\ -f_2 \tan\theta \\ 0 \end{bmatrix} \tag{2.6}$$

where $-f_2 \tan\theta$ represents the tilting translation after adjusting the sign in RCS.

2.3 Windowing Effect

Although the magnification M is determined solely by the focal lengths of lenses in the system, such advantage comes with a tradeoff: the truncation of transmit pixels visible to the receiver. This truncation occurs due to the limited angular

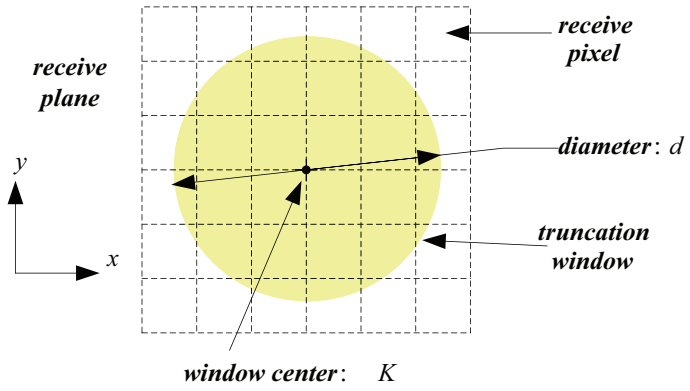

Figure 2.5: Parameters of the Truncation Window in Pixelated MIMO Channel

subtense of the receive lens by its finite aperture. Such effect is described by a 2-dimensional window function $w(x, y)$ defined over domain $\mathcal{W}$ in the RCS. Given that most commercial lenses are circular in shape and the truncation window is merely a projection of the receive lens, we assume the domain $\mathcal{W}$ to be circular as well. To parameterize this domain over which the window function is defined, its diameter and center are discussed in the following sections. As Fig. 2.5 shows, the diameter of the circular domain $\mathcal{W}$ is denoted by d and the center of the circle is denoted by point K. The notation with capital letter $K(x, y)$ is used to represent a point and its corresponding coordinates. The notation with lowercase letter $w(x, y)$ is used to denote a 2-dimensional function with x, y as variables.

2.3.1 Window Diameter

Fig. 2.6 describes a cross-sectional view of the system in the general case where the diameter d of the circular domain $\mathcal{W}$ is determined. This cross-sectional view is chosen to be the plane formed by the two optical axes of both lenses.

Point A, B are the source points on the y-axis of TCS. Due to the limited angular

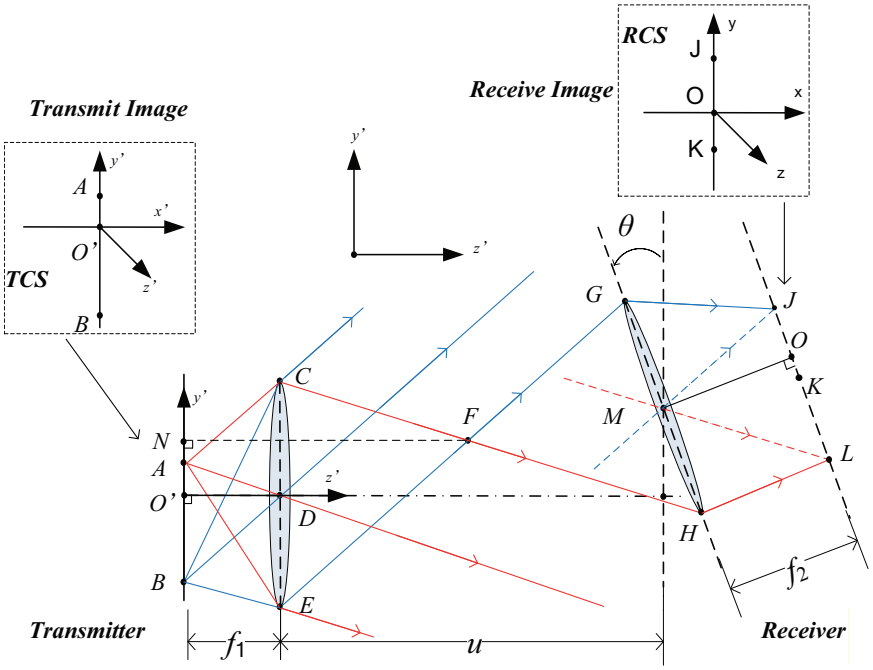

Figure 2.6: Calculation of Window Parameters (General Case)

subtense of the receive lens, all rays emitted from points A, B cannot all be captured by the receive lens. As shown in Fig. 2.6, only rays which segment EG, CH lie in can be considered to be captured by the edge of the receive lens. According to ray optics, the corresponding image points of A and B are found as L and J on the image plane.

In this cross-sectional view, considering point sources outside segment AB on the y-axis in transmit image, the angles of rays they emit relative to the optical axis of the receive lens increase on both sides outside segment AB correspondingly. Therefore, rays emitted from all the points on y-axis outside AB in Fig. 2.6 will not be captured by the receiver. Therefore, point A, B can be considered to be on the "edge" of the transmit image viewable to the receiver. Correspondingly, their image points L, J can be considered on the edge of the viewable region on the image plane since the receive pixels outside segment LJ along the axis in the figure will not receive any rays

from the transmitter. According to the assumption that $\mathcal{W}$ is circular in shape and symmetric to the y-axes (point L, J are both on y-axis of RCS), the diameter of the window can be written as $d = |LJ|$. In Fig. 2.6, the center K of the domain $\mathcal{W}$ can also be found by assuming $|JK| = |KL|$.

In Fig. 2.6, in relation to the origin of TCS O', positions of point C, D, E, G, M, H, O all can be written with coordinates of TCS. A simple guideline is provided on how to calculate the window diameter $d = |LJ|$. Details of the calculation process are discussed in Appendix A. The key steps to compute the window diameter can be summarized as follows.

(1) Compute the line equations of lines in which segments CH, EG lie with known coordinates of C, H, E, G in TCS.

(2) Compute the coordinates of intersection point F with line equation of CH, EG in TCS.

(3) In similar triangle pair $\triangle FCE \sim \triangle DAB$, we have $(|FN| - |O'D|)/|O'D| = |CD|/|AB|$. $|AB|$ can be obtained with known $|FN|, |O'D|, CD|$.

(4) Combine $|AB|$ with (2.4), $d = |LJ| = M|AB| = \frac{f_2}{f_1}|AB|$.

Follow the guideline above, the diameter d of the domain $\mathcal{W}$ is finally determined to be:

$$d = \frac{f_2(ul_r \cos\theta + ul_t + |\vec{\delta}|l_r \sin\theta)}{u^2 - \frac{l_r^2 \sin^2\theta}{4}} \tag{2.7}$$

where $\theta \in [0, \pi/2)$ and $u > l_r/2$.

2.3.2 Window Center

The center of the circular domain $\mathcal{W}$ in Fig. 2.6 is defined as point K. Since K lies on the y-axis of the RCS, $K(0, y_p)$ is used to denote its coordinates in RCS.

In the general case described in Fig. 2.6, since the diameter $d = |JL|$ of $\mathcal{W}$ is already computed in Section 2.3.1 in (2.7), $|OK|$ can be found through $|OK| = |JK| - |JO| = 0.5d - |JO|$. Therefore, the coordinate of window center in RCS is $K(0, -|OK|)$.

Similar to Section 2.3.1, in Fig. 2.6, the coordinates of points C, D, E, G, M, H, O can be written in TCS. To find the window center $K(0, y_p)$, geometric relationships in Fig. 2.6 are used based on ray optics. Details of the calculation are also provided in Appendix B. A brief summary of the steps used to find the window center is listed as follows:

(1) Compute the line equations of lines in which segments GH, GE lie with known coordinates of G, H, C, E in TCS.

(2) Use parallel relations $EG \parallel MJ, GH \parallel JO$ and known coordinates of points M, O, line equations of MJ, JO can be computed.

(3) Compute the coordinate of intersection point J with line equations of MJ, JO in TCS.

(4) Compute the length of segment JO with know coordinates of point J and O in TCS as $|JO|$.

(5) Notice that $|JK| = 0.5d$. Therefore, we have $|OK| = |JK| - |JO|$.

The computed value of $|OK|$ is combined with $K(0, -|OK|)$ to obtain the window center coordinates in RCS.

Thus, by adjusting the sign, the window center can be found as $K(0, y_p)$ in RCS,

where

$$
\begin{aligned}
y_p = &- \frac{f_2(ul_t + |\vec{\delta}|l_r \sin\theta + ul_r \cos\theta)}{2(u^2 - \frac{l_r^2 \sin^2\theta}{4})} + ((|\vec{\delta}| + f_2 \sin\theta(l_r f_2 \cos^3 + 2|\vec{\delta}| f_2 \cos^2\theta \\
&+ f_2 l_t \cos^2\theta + |\vec{\delta}| l_r^2 \sin\theta\cos\theta - |\vec{\delta}| l_r \sin\theta\cos\theta + 2u|\vec{\delta}|\cos\theta + l_r^2 f_2 \sin^2\theta\cos\theta \\
&+ 2|\vec{\delta}|^2 l_r \sin\theta + 2|\vec{\delta}| l_r f_2 \sin^2\theta + |\vec{\delta}| l_t l_r \sin\theta + l_t l_r f_2 \sin^2\theta)(2u\cos\theta + l_r^2 \sin\theta\cos\theta \\
&- l_r \sin\theta\cos\theta + 2|\vec{\delta}| l_r \sin\theta + l_t l_r \sin\theta)^{-1})^2 + (u + f_2\cos\theta - (2u^2\cos\theta \\
&- l_r^2 f_2 \sin^3\theta + 2u f_2 \cos^2\theta - u l_r \sin\theta\cos\theta + 2|\vec{\delta}| u l_r \sin\theta + u l_t l_r \sin\theta \\
&- l_r f_2 \sin\theta\cos^2\theta + u l_r^2 \sin\theta\cos\theta + 2u l_r f_2 \sin^2\theta)(2u\cos\theta + l_r^2 \sin\theta\cos\theta \\
&- l_r \sin\theta\cos\theta + 2|\vec{\delta}| l_r \sin\theta + l_t l_r \sin\theta)^{-1})^2)^{\frac{1}{2}}.
\end{aligned}
\tag{2.8}
$$

2.3.3 Special Case

In the general case, the computed window center and diameter are shown to consist of numerous terms. In this section, the special case where $\theta = 0$ is discussed. Fig. 2.7 depicts this case where the transmit plane and receive plane are considered to be parallel.

The diameter d is determined geometrically by the extremal angles which are subtended by the receive lens. In particular, using the similar triangle relation $\triangle EFG \sim \triangle EJH$ gives $|HJ| = (l_t + l_r) f_1/u$. Applying the magnification in (2.4) gives

$$
d = \frac{f_2(l_t + l_r)}{u}. \tag{2.9}
$$

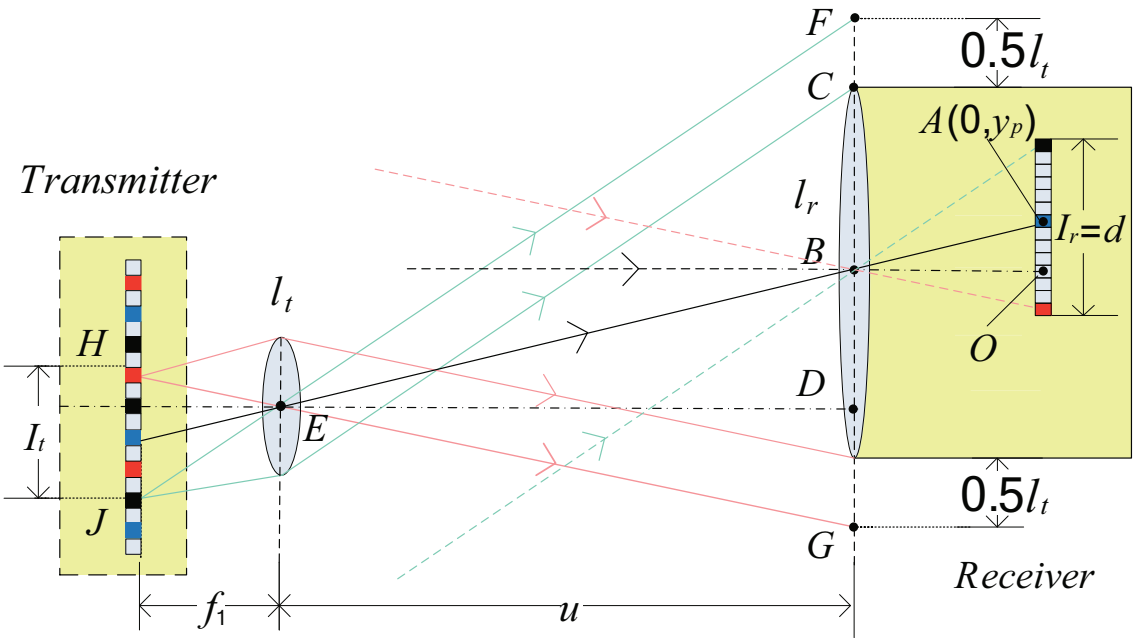

Figure 2.7: Calculation of Window Parameters (Special Case)

This result is in accordance with (2.7) by applying $\theta = 0$.

Analogously, the center of the window in this case is merely the projection of the transmit pixel which connects the optical centers of the transmit and receive lenses onto the receive plane. Denote the window center as $K(0, y_p)$ in RCS similar to previous analyses. In similar triangle pair $\triangle ABO \sim \triangle BED$, we have the relation $|AO|/|BD| = |BO|/|DE|$. Therefore, simple algebra yields

$$|y_p| = |AO| = \frac{|BD||BO|}{|DE|} = \frac{f_2|\vec{\delta}|}{u}. \tag{2.10}$$

After adjusting the sign, the coordinate of window center in RCS is found to be: $K(0, \frac{f_2|\vec{\delta}|}{u})$. This result also obeys (2.8) when $\theta = 0$ is applied.

In practice, when θ is considerably small, the expressions in special case can be used to approximate the general case to simplify the expression.

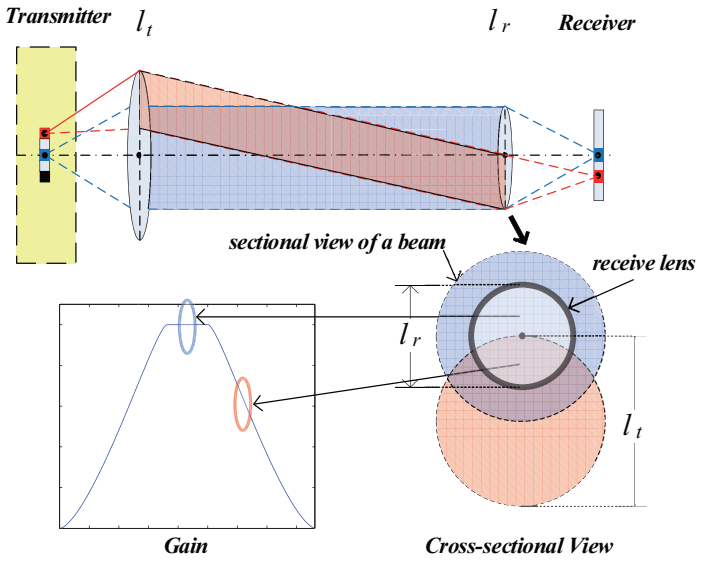

Figure 2.8: Calculation Process of the Window Gain

2.3.4 Window Gain

Defined in RCS, the value of $w(x, y)$ within the domain $\mathcal{W}$ is affected by various factors in the channel: the spatial intensity distribution of the transmit pixel, the different path loss of the optical signal, the numerical aperture of the receive lens, and different amount of power received due to limited apertures of both lenses.

Under certain assumptions, the gain of the window is primarily determined by the number of ray bundles received at a particular angle. Assume each transmit pixel emits intensity isotropically. The light transmitted from a given transmit pixel is assumed to leave the collimating lens as a cylindrical beam with a uniform power distribution if path loss is not considered.

The intersection of a portion of the cylindrical transmit beam by the receive lens results in a variation of gain over the domain for $w(x, y)$, which can be found by ray tracing as Fig. 2.8 indicates. Due to the fixed aperture l_r, only a smaller limited portion of the red beam is captured by the receiver compared to the blue one. In the

cross-sectional view of the beams, since power distribution is assumed to be uniform, the different amount of power captured in regard to individual transmit pixel by the receiver is proportional to the area of the intersection part of each cylindrical beam with the receive lens. The computation of window gain differs slightly based on the relation of l_t, l_r.

One example of the case where $l_r < l_t$ is computed when $\theta = 0, |\delta| = 0$ (The details are included in Appendix C). Notice that in this case the gain is symmetric to the origin of RCS, to simplify the calculation, only power accumulated along one window diameter is examined. The overall gain can be obtained by integration over $\mathcal{W}$. The window gain $w(0, y) =$

$$
\begin{cases}
\frac{l_r^2}{4}\arccos\frac{\frac{u^2y^2}{f_2^2}+\frac{l_r^2}{4}-\frac{l_t^2}{4}}{\frac{-ul_ry}{f_2}} - \frac{l_r^2}{8}\sin 2\arccos\frac{\frac{u^2y^2}{f_2^2}+\frac{l_r^2}{4}-\frac{l_t^2}{4}}{\frac{-ul_ry}{f_2}} & \\
+\frac{l_t^2}{4}\arccos\frac{\frac{u^2y^2}{f_2^2}+\frac{l_t^2}{4}-\frac{l_r^2}{4}}{\frac{-ul_ty}{f_2}} - \frac{l_t^2}{8}\sin 2\arccos\frac{\frac{u^2y^2}{f_2^2}+\frac{l_t^2}{4}-\frac{l_r^2}{4}}{\frac{-ul_ty}{f_2}}, & \frac{-f_2l_t-f_2l_r}{2u} < y < \frac{-f_2\sqrt{l_t^2-l_r^2}}{2u} \\
\frac{l_r^2}{4}\arccos\frac{\frac{u^2y^2}{f_2^2}+\frac{l_r^2}{4}-\frac{l_t^2}{4}}{\frac{-ul_ry}{f_2}} + \frac{l_r^2}{8}\sin 2(\pi-\arccos\frac{\frac{u^2y^2}{f_2^2}+\frac{l_r^2}{4}-\frac{l_t^2}{4}}{\frac{-ul_ry}{f_2}}) & \\
+\frac{l_t^2}{4}\arccos\frac{\frac{u^2y^2}{f_2^2}+\frac{l_t^2}{4}-\frac{l_r^2}{4}}{\frac{-ul_ty}{f_2}} - \frac{l_t^2}{8}\sin 2\arccos\frac{\frac{u^2y^2}{f_2^2}+\frac{l_t^2}{4}-\frac{l_r^2}{4}}{\frac{-ul_ty}{f_2}}, & \frac{-f_2\sqrt{l_t^2-l_r^2}}{2u} \leq y <\leq \frac{+f_2l_r-f_2l_t}{2u} \\
\frac{\pi l_r^2}{4}, & \frac{+f_2l_r-f_2l_t}{2u} < y < \frac{+f_2l_t-f_2l_r}{2u} \\
\frac{l_r^2}{4}\arccos\frac{\frac{u^2y^2}{f_2^2}+\frac{l_r^2}{4}-\frac{l_t^2}{4}}{\frac{ul_ry}{f_2}} + \frac{l_r^2}{8}\sin 2(\pi-\arccos\frac{\frac{u^2y^2}{f_2^2}+\frac{l_r^2}{4}-\frac{l_t^2}{4}}{\frac{ul_ry}{f_2}}) & \\
+\frac{l_t^2}{4}\arccos\frac{\frac{u^2y^2}{f_2^2}+\frac{l_t^2}{4}-\frac{l_r^2}{4}}{\frac{ul_ty}{f_2}} - \frac{l_t^2}{8}\sin 2\arccos\frac{\frac{u^2y^2}{f_2^2}+\frac{l_t^2}{4}-\frac{l_r^2}{4}}{\frac{ul_ty}{f_2}}, & \frac{f_2l_t-f_2l_r}{2u} \leq y \leq \frac{f_2\sqrt{l_t^2-l_r^2}}{2u} \\
\frac{l_r^2}{4}\arccos\frac{\frac{u^2y^2}{f_2^2}+\frac{l_r^2}{4}-\frac{l_t^2}{4}}{\frac{ul_ry}{f_2}} - \frac{l_r^2}{8}\sin 2\arccos\frac{\frac{u^2y^2}{f_2^2}+\frac{l_r^2}{4}-\frac{l_t^2}{4}}{\frac{ul_ry}{f_2}} & \\
+\frac{l_t^2}{4}\arccos\frac{\frac{u^2y^2}{f_2^2}+\frac{l_t^2}{4}-\frac{l_r^2}{4}}{\frac{ul_ty}{f_2}} - \frac{l_t^2}{8}\sin 2\arccos\frac{\frac{u^2y^2}{f_2^2}+\frac{l_t^2}{4}-\frac{l_r^2}{4}}{\frac{ul_ty}{f_2}}, & \frac{f_2\sqrt{l_t^2-l_r^2}}{2u} < y < \frac{f_2l_t+f_2l_r}{2u}
\end{cases}
\tag{2.11}
$$

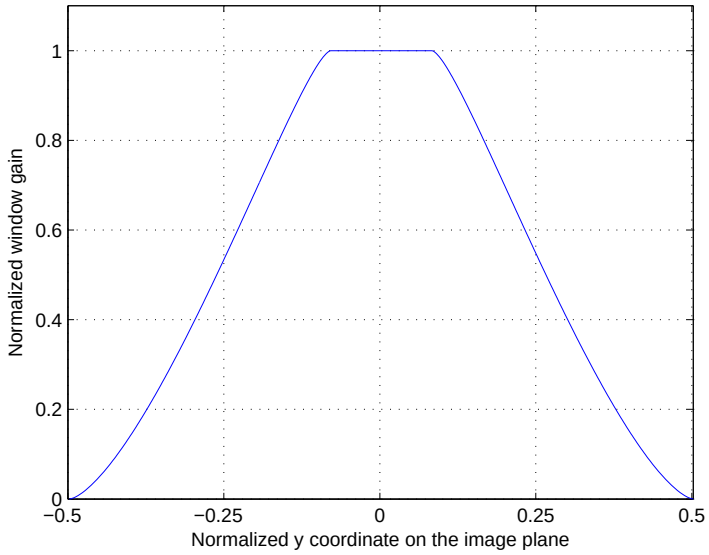

Figure 2.9: Simulation of one example of Normalized Gain Function, only values along the diameter $x = 0, y \in [-0.5, 0.5]$ is plotted.

In particular, Fig. 2.9 plots the window gain along one diameter of the circular domain based on (2.11). Parameters from the experimental setup in Table 4.1 are used initially for computation. The gain is normalized by its maximum value and y coordinates are normalized by the diameter of the domain $\mathcal{W}$. The theoretical curve in Fig. 2.9 is flat near the center since the entire receive lens is projected onto the image plane. In the case where $l_r > l_t$, the center would also be flat since the entire transmit lens is imaged onto the receiver.

Notice that this gain function does not take a host of other important factors into consideration. As stated before, the path loss, the numerical aperture and the spatial intensity distribution of the transmit pixel all affect the gain of the window. Therefore, a complete characterization of the gain function is difficult but it can be measured accurately in experiments.

2.4 Point Spread Function and Noise

A brief introduction of the point spread function and noise is presented in this section based on the proposed channel model.

2.4.1 Point Spread Function

In an incoherent optical system, the imaging system can be considered as a linear system in intensity [63]. As impulse response is often used in wireless communications to characterize a channel, the point spread function is introduced similarly to describe the channel property of an imaging system. Defined as the channel response of a spatial impulse in the imaging system, the PSF will result in a blurring receive image compared to the transmitted one and serves as an important indicator of the imaging quality of the whole system [45].

According to [63], the image formation process can be separated into two major steps based on linear system theory. The transmitted image is firstly magnified and translated onto the image plane, PSF is then convoluted with the image to obtain the final receive image. In the fixed-scale pixelated MIMO channel, since the windowing effect will result in partial loss of the transmit pixels, the magnified image is firstly truncated before the convolution.

According to scalar diffraction theory [63], the PSF is often modeled as an spatial-invariant low-pass filter. Note that in our case, the PSF will change when the camera is off-axis. When the operation is near the axis where θ and $|\delta|$ are considerably small, the system can be approximated to be spatial-invariant. Although limited by aperture effects, the PSF is also affected by a host of other effects such as distortion and wavelength changes. The corresponding Fourier Transform of the PSF is termed

optical transfer function (OTF) and is often used to characterize the channel in spatial frequency domain. According to [63], the OTF of the imaging system is mostly limited by the diffraction and can be roughly modeled as a 2-dimensional Gaussian shape curve. Measurements in [64] also verified such assumption. As a well established method, the PSF of an imaging system is mostly measured through experimental results [40].

2.4.2 Noise

The noise in an imaging system consists of both signal-dependent and signal-independent noise. According to the source from which the noise is generated, the noise can be categorized briefly as:

(1) Thermal noise: The thermal noise of an imaging system comes mainly from readout and reset transistors [40]. Due to the thermal effect in the circuit, thermal noise is considered signal independent. According to [64], thermal noise can be modeled as Gaussian distribution with zero mean. This noise becomes dominant when low illumination occurs according to [40].

(2) Shot noise: In an imaging system, due to the discrete nature of energy and charge in the photodiode [64], shot noise is present. Both ambient light and transmit signal can give rise to shot noise [64]. Being signal independent, the ambient light shot noise dominates when intense background illumination exists. When high illumination is provided from the transmit signal, signal dependant shot noise dominates. The distribution of shot noise is often described by Poisson distribution [65]. Applying the central limit theory, when a large number of photons are present, the overall distribution of shot noise can be approximated by a

Gaussian distribution.

(3) Fixed pattern noise: Fixed pattern noise arises from spatial nonuniformity and defect pixels in a sensor array [66]. Variations in pixel size, interference with local circuitry and nonuniform sensitivity can all cause fixed pattern noise [67]. Under longer exposure time, fixed pattern noise can result in degradation of image quality. Since numerous existing methods [67] can suppress the fixed pattern noise, it is not considered in this system.

2.5 Communication Model

In this section, an end-to-end mathematical communication model is presented. The number of visible transmit pixels at the receiver is also computed and discussed.

2.5.1 Overall Model

An overall system model is shown in Fig. 2.10. For simplicity, in the balance of the thesis we restrict $\theta = 0$ and δ to be small. The model can be easily generalized in practice and, as will be shown in Chapter 4, the prototype system is robust over different positions of the receiver and transmitter. What worth noticing here is that for all points on the transmit image plane or receive image plane, the z coordinates are all 0. therefore, instead of using the full notation (x, y, z) to denote the coordinates of a point, (x, y) is used in both RCS and TCS by removing the z coordinate.

Assume the receiver and transmitter are synchronized in time. A receive frame consists of $n_r \times n_r$ pixels spaced at D_r and the corresponding single transmit frame consists of $n_t \times n_t$ pixels spaced at D_t from each other. Moreover, assume that the

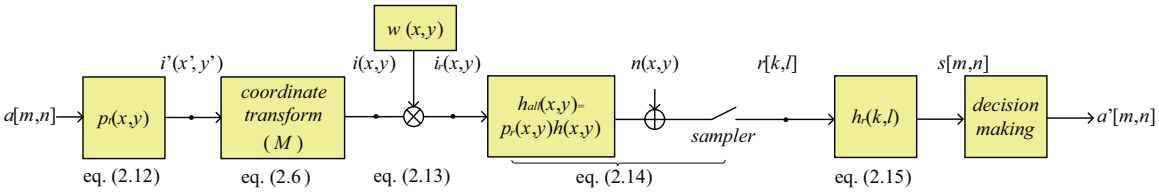

Figure 2.10: The Block Diagram for Fixed-scale MIMO VLC System

center of the transmit image, i.e., O', is in the center of a transmit pixel (when n_t is odd) or the intersection point of four neighboring pixels (when n_t is even). Let $i'(x', y')$ denote the transmitted image and define $p_t(x', y')$ as the transmit pixel aperture function which is assumed to be identical for each transmit pixel. The data assigned to the transmit pixels are denoted as $a[m, n] \in \{0, 1\}$ where $m, n \in [0, n_t - 1]$. The transmit image can then be written as:

$$i'(x', y') = \sum_{m=0,n=0}^{n_t-1,n_t-1} a[m, n] p_t \left(x' - mD_t + (n_t - 1)\frac{D_t}{2}, y' - nD_t + (n_t - 1)\frac{D_t}{2} \right). \tag{2.12}$$

The mapping between TCS and RCS in (2.6) can then be applied to yield the corresponding image $i(x, y)$. The impact of the finite angular subtense of the receiver will window the received image, as discussed in Section 2.3. The resulting received image, $i_r(x, y)$, after windowing is

$$i_r(x, y) = w(x, y)i(x, y). \tag{2.13}$$

Let $h(x, y)$ denote the overall PSF of the optical system and $p_r(x, y)$ denote the receive pixel aperture assumed to be identical for all receive pixels. The combined channel response considering both effects is $h_{\text{all}}(x, y) = h(x, y) * p_r(x, y)$ where $*$ denotes two-dimensional convolution. In practice, since the receive pixel is much

larger than the PSF of the imaging system, $h_{\text{all}}(x,y) \approx p_r(x,y)$. Again, it is assumed that the origin of the image plane is either at the center of a receive pixel (when n_r is odd) or the intersection of four neighboring pixels (when n_r is even) to ensure symmetry. The receive imager integrates the intensity over each pixel and outputs an estimate $r[k,l]$

$$r[k,l] = i_r(x,y) * h_{\text{all}}(x,y)|_{\substack{x=-kD_r+(n_r-1)\frac{D_r}{2} \\ y=-lD_r+(n_r-1)\frac{D_r}{2}}} + n[k,l] \tag{2.14}$$

where $k,l \in [0, n_r - 1]$. The noise samples are assumed to be i.i.d and Gaussian. Noting the intense background illumination, only signal independent noise is considered.

In most cases, the receiver array has a large number of pixels which oversample the received image. That is, each transmit pixel is oversampled and captured by a set of receive pixels. With this added degree of freedom, the receiver can perform spatial synchronization to determine the location of each transmit pixel in $\mathcal{W}$ and perform spatial filtering to provide a detection statistic for each transmitted sub-channel, $s[m,n]$. More precisely,

$$s[m,n] = r[k,l] \otimes h_r[k,l]|_{k,l \in \mathcal{Q}} \tag{2.15}$$

where $h_r[k,l]$ is the receive filter and $\mathcal{Q}$ is the set of locations for each transmit pixel determined through spatial synchronization.

The $s[m,n]$ are sent to a decision making module to determine estimates of the transmitted data for each sub-channel denoted as $a'[m,n]$.

2.5.2 Tradeoffs

Consider the problem of estimating the number of sub-channels available between the transmitter and receiver for a given distance and position. Using the notation of Section 2.5.1, let $|\mathcal{Q}|$ denote the number of transmit pixels that are imaged within the domain of windowing function, $\mathcal{W}$, at the receiver. Given that the transmit pixel is a square with D_t length sides, the number of transmitter pixels visible to the receiver can be estimated as,

$$|\mathcal{Q}| \approx \frac{|\mathcal{W}|}{D_t^2 M^2} = \frac{\pi}{4} \cdot \frac{{f_2}^2 (l_r + l_t)^2}{u^2 D_t^2 M^2} = \frac{\pi {f_1}^2 (l_r + l_t)^2}{4u^2 D_t^2}. \tag{2.16}$$

There are several notable tradeoffs this approximation raises for system design.

1. A larger f_1 is preferred to obtain a larger viewable region at a fixed distance which increases the number of viewable transmit pixels at the receiver. However, from (2.4), increasing f_1 for a fixed f_2 reduces the magnification of the system. This results in a smaller oversampling rate of transmit pixels at the receiver making spatial synchronization more difficult.

2. For a given system, according to (2.9), $|\mathcal{W}| \propto \frac{1}{u^2}$. Hence, the closer the camera is, the more sub-channels can be captured with no truncation, thus a higher data rate is available.

3. When the camera moves on the same plane at a fixed distance, $|\mathcal{W}|$ is not impacted and neither is $|\mathcal{Q}|$. This is a consequence of spatial-angular mapping from the lens. However, changing $\vec{\delta}$ can result in different window positions according to (2.10).

4. From (2.16), the number of viewable transmit pixels increases greatly with increasing lens sizes (i.e., l_t and l_r). However, practical constraints on lens sizes and form factors of the receiver and transmitter will constrain this choice.

These tradeoffs will be considered in our system design process presented in Chapter 3.

2.6 Summary

This chapter presented a detailed model of the fixed-scale pixelated MIMO VLC channel. The magnification of the system is determined to be constant and dependent solely on the focal lengths of the transmit and receive lenses. Such feature is the key to this system and an indoor optical data broadcasting system with multiple simple receivers can be implemented based on this advantage. In the case where receiver changes in orientation and position, the model is also shown to be robust, thus not requiring strict alignment. The truncation window of the channel is also parameterized by its center, diameter and gain in both general and special cases. With knowledge of this truncation window, the erasure of sub-channels can be predicted and the data transmission scheme can be modified to further improve system performance. An overall communication model is given based on previous analyses. By examining the visible sub-channels in this model, theoretical frameworks are provided for system design. Chapter 3 will provide details on how to select the proper transmitters, receivers and lenses in order to achieve a proper magnification as well as a higher data rate based on this model.

Chapter 3

System Design

In this chapter, a guide on the design of the fixed-scale pixelated MIMO VLC system is presented. Selection of components and their associated parameters is firstly discussed. Since the system performance largely depends on the components used, the design guide follows the principal of balancing between cost and performance. Therefore the analyses are mainly based on the parts that are commercially available. Examples are then given to demonstrate this design process. Due to the truncation window described in Section 2.3, Raptor 10 code is applied and the corresponding packet arrangements of the code are investigated. The potential for localization benefits of this system is also briefly discussed at last. This extra advantage can be exploited in the future to design a hybrid communication and localization system.

3.1 System Design and Parameter Selection

3.1.1 Transmitter Selection

As mentioned in Section 2.1, the transmitter is a multi-element optical intensity emitter which is able to generate different coded images by addressing and modulating each element (pixel) independently.

Several types of image displays based on different technologies can be considered as potential transmitters of this system. To select the proper transmitter, some important parameters are of great interest to the designers: the pixel size (D_t) of each transmit pixel, resolution, brightness, viewing angle (spatial performance) and response time (temporal performance) [68]. By examining these parameters of different types of transmitters, the designer should balance between the cost and performance when making a decision.

The most common option is an liquid-crystal display (LCD). An LCD consists of two parts: an LCD panel and a backlight module. The LCD panel is a layer of liquid crystal molecules surrounded by two layers of optical polarizing filters. The polarization directions of the two filters are perpendicular to each other [68]. Since the LCD panel is not a light source, arrays of white LEDs, termed backlight, are used to provide illumination. When no electrical field is added to the liquid crystal molecules, light emitted from the backlight cannot pass the second polarizing filter since its polarization direction is perpendicular to the filter. When external electrical field is active, the liquid crystal molecules are twisted [69]. Light from the backlight module is then rotated and passes the second filter. When different voltages are fed at different positions, only a portion of the pixels allow light to pass. Therefore,

different images can be displayed accordingly.

The most attractive advantage of LCDs is that they are commercially available at lower prices. Widely used as computer monitors and TV displays, an LCD with resolution of around 2000×1000 and refreshment rate around 60 Hz can be purchased at round 95.3 USD [70]. Moreover, LCDs enjoy the benefit of lower energy consumption and thinner shapes than most conventional displays like cathode ray tube (CRT) displays [71]. However, one drawback of LCDs is their limited viewing angles. Most LCDs have viewing angles around 45 degrees (or even less) from the normal of the panel. When moving beyond viewing angles, the picture quality drops drastically and only half of the contrast ratio can be achieved according to [72].

Another possible choice is organic light-emitting diode display (OLED). Different from LCDs, OLEDs are based on organic layers between two electrodes [73]. In response to external voltages, the OLED panel can emit light itself without a backlight module [74]. Compared to LCDs, OLEDs enjoy advantages such as larger viewing angle (over 80 degrees from the normal), better contrast ratio and faster response time [75]. However, since it is comparatively newly introduced, most OLEDs are still only available at higher prices. What's more, currently OLEDs also suffer from lower lifespans compared to LCDs [76], especially, blue OLEDs only have lifespan around 14000 hours.

Displays using LED arrays or even laser arrays based on vertical-cavity surface-emitting lasers (VCSEL) can also serve as potential transmitters of the system. With each single LED as one pixel, arrays of LEDs are arranged onto a printed circuit board (PCB). Due to the physical size of each LED (on the order of 1 mm) [77], LED

Table 3.1: Comparison of Various Transmitters [79, 82]

Type	LCD	OLED	μLED
viewing angle (degree)	45	80	80
response time	ms	μs	ns
pixel size D_t	200μm	200μm	10 μm
backlight	yes	no	no
lifespan	medium	medium	long
price	low	medium	high

arrays are mostly available at larger sizes [78]. Widely used in traffic signal systems and outdoor screens, LED arrays can be used for illumination or decoration while working as data transmitters.

One problem with LED displays is the physical size of each LED will reduce the viewable pixel number at the receiver according to (2.16). However, the newly emerged μLED technology can provide a smaller physical dimension (around 10μm [79, 80]) while ensuring each LED (pixel) can be independently driven at high speed. The performance of μLED display is superior than most other types of displays [81]. However, since there are few commercially available μLED displays, such transmitters can only be considered as primary choice in the near future.

In Table 3.1, key parameters of different potential transmitters are compared.

3.1.2 Receiver Selection

In the fixed-scale pixelated MIMO wireless optical system, the receiver is generally considered to be a camera with good imaging quality at higher frame rate. Two mainstream technologies of camera sensors are charged-coupled device (CCD) and Complementary Metal-Oxide-Semiconductor (CMOS).

The CCD image sensor is based on an array of capacitors. When a image is

received by the array, electrical charges are accumulated in each individual capacitor. Similar to a shift register, the control circuit is activated to transfer the charges from one capacitor to its neighbour. The charges are then sent into amplifiers and digitizers sequentially. Since the charges are converted to digital signals with small number of output nodes, the resulting images often enjoy less noise and higher image quality [83].

Compared to CCD sensors, CMOS sensors integrate analog-to-digital converter (ADC) units and amplifiers in each individual pixel. Such parallel structure offers a faster readout speed compared to CCD sensors [84]. Additionally, CMOS cameras allow for a "region of interest" (ROI) sampling [85]. When only a smaller portion of the frame needs to be sampled, the corresponding operating frame rate of the camera can be increased thanks to the parallel ADCs and amplifiers. Such advantage is attractive when flexible readout and higher frame rates are preferred, as in our pixelated MIMO system. The control circuit of CMOS camera can also be easily integrated on a chip, such advantage makes the sensor array more power efficient compared to CCD [84]. However, additional logic in each individual pixel reduces the active pixel area of the CMOS camera. The disparities between each pixel and its local circuitry will also result in more fixed pattern noise compared to CCD sensors [84].

3.1.3 Lens Selection

The selection of the optical parameters of both transmit and receive lenses will impact the performance of the system. In particular, l_r ,l_t, f_1 and f_2 must be selected to maximize the number of sub-channels while maintaining a practical implementation.

Following (2.4), the system magnification is solely determined by f_1 and f_2 and is independent of u. Define the spatial oversampling ratio (OSR) as the number of receive pixels corresponding to each transmit sub-channel, i.e.,

$$\text{OSR} = M^2 \frac{D_t^2}{D_r^2} = \frac{f_2^2}{f_1^2} \frac{D_t^2}{D_r^2}. \tag{3.1}$$

OSR must be selected to be large enough to allow for spatial registration of the transmit image by the receiver. Clearly, the selection of M via the ratio of focal lengths must be done to ensure the OSR is as small as possible for more visible sub-channels while ensuring spatial synchronization.

Following (2.16), the number of visible sub-channels between the receiver and transmitter is maximized by choosing the largest possible focal length f_1 and apertures, l_t and l_r. In practice, however, both commercial lenses and form factor constraints limit the freedom with which optical parameters can be selected.

According to (2.7) and (2.16), larger l_t and f_1 are always ideal for more received sub-channels. The transmit lens is mostly limited by its cost to find a larger f_1, l_t. Most optical lenses are based on glass, plastic or other synthetic materials. They are most commercially available in small sizes with good imaging qualities according to [86].

An alternative option is the Fresnel lens. Different from traditional lenses, a Fresnel lens divides the lens into a set of co-centered circular sections to obtain a flat surface. Compared to traditional lens, Fresnel lenses are less expensive with significantly larger apertures. However, since the Fresnel lens replaces a smooth surface with numbers of small sections, usually the image quality is greatly degraded [87]. So in cases where receive image quality is the primary consideration, Fresnel

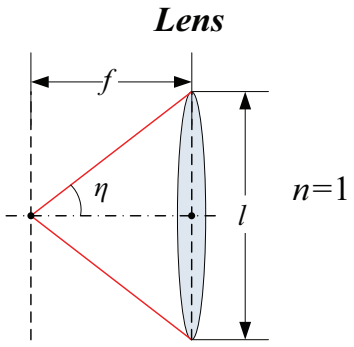

Figure 3.1: Numerical Aperture

lens may not be a very good choice.

When selecting the receive lens, according to (2.7) and (2.16), larger l_r is often preferred. Considering the receiver being a camera, most receive lens are commercial lenses designed specially for cameras.

One important parameter for these receive lenses is the f-number N. The f-number of a camera lens is defined as the ratio between focal length f and aperture size l: $N = f/l$. Most commercial lenses have f-numbers in the range of 1 to 11.3, in increasing powers of $\sqrt{2}$.

Another important parameter is the numerical aperture (NA). Although in our model in Section 2.1, the receive lens is assumed to be able to collect light from any direction from its optical axis, in practice, a camera lens can only receive light within a certain angle in regard to its optical axis. In photography, NA is used to describe such angles. As shown in Fig. 3.1, NA is defined as: $NA = n \sin \eta$, where η is half of the maximum acceptance angle in regard to focal point O and n is the refraction index of the media. When camera is focused at infinity and the media is assumed to be in the air, $n = 1$, NA can be connected with f-number by:

$$NA = n \sin \eta = \sin \arctan \frac{l}{2f} \approx \frac{l}{2f} = \frac{1}{2N}. \tag{3.2}$$

Notice such approximation is valid only with small η. However for larger NA, such approximation can still hold according to [88]. Therefore, to ensure a larger NA is available, the designer should choose a smaller f-number for the receive lens. Although f_1 is shown not to directly affect the number of sub-channels received and one needs to look for a larger l_r of the receive lens when M is sufficiently large for synchronization, larger f_1 is still preferred with a smaller f-number.

In many cases, the receiver may be a camera in a mobile device which has strict constraints on focal lengths and aperture sizes available. Considering the proposed system is a "broadcasting system", it is reasonable to concentrate more on the transmitter end. At the transmitter, lenses with large diameter l_t and focal length f_1 increase the number of sub-channels and high-quality commercial single element lenses are typically available at diameters less than 50 mm [86]. As stated before, larger aperture Fresnel lenses are available, however, their imaging quality is lower than conventional optical lenses.

3.2 Design Examples

In this section, two rough examples are given to demonstrate the design process by selecting different components.

The first example uses transmitter based on μLED arrays. Consider a receiver is based on a smart phone camera which typically has $f_2 \approx 4$ mm, f-number≈ 2 and $D_r \approx 1$ μm. The transmitter can be realized using an array of μ-LEDs [80]

with $D_t \approx 20$ μm. To simplify spatial registration, let OSR ≈ 10. Using (3.1) gives $f_1 \approx 25.3$ mm (i.e., one inch).

To maximize data rate, l_t, should be chosen as large as possible. Commercial high-quality single element lenses are available with f-number near 1, giving $l_t \approx 25.4$ mm. Substituting into (2.16) gives an array of approximately 945 sub-channels available at transmission distance of 1 m.

Another example will be based on the experimental setup presented in Section 4.1. The transmitter is based on an LCD with pixel pitch $D_t \approx 294$ μm. The receiver is chosen as a high-speed CMOS camera with pixel size $D_r \approx 12$ μm. The receive lens associated with the camera has a focal lens $f_2 = 25$ mm and f-numbers available from $1.4 - 22$. To maximize the receive lens aperture l_r, 1.4 is chosen and thus l_r is determined to be 17.9 mm.

The transmit lens is selected as a double-convex lens, with the focal lens $f_1 = 50$ mm and $l_t = 50$ mm. With an camera digitizer factor of 2, the OSR are then calculated as OSR $= (\frac{2D_t f_2}{D_r f_1})^2 \approx 600$. Substituting into (2.16) gives an array of approximately 26 sub-channels available at transmission distance of 1 m.

The examples discussed above show that component and parameter selection can affect the system performance greatly. Same as (2.16) predicts, by choosing transmitters with smaller pixel size, a higher potential data rate is expected when spatial synchronization is ensured.

3.3 Raptor Codes

Although the scale of the pixelated MIMO VLC system is fixed, different window diameters and centers will truncate the images in different locations depending on the

range and device position. Here we use a fountain code over the transmitted pixels to track changes in window truncation while maintaining a reliable communication link.

Firstly introduced in [89], fountain codes are used for erasure channel where reliable data delivery is required due to the potential packet loss. For a given source block of data, the fountain code encoder is able to produce infinite numbers of encoded symbols. The decoder, on the other hand, is able to decode the original information successfully as long as sufficient number of encoded symbols are collected correctly, regardless of the order of the received encoded symbols. Since the encoder can generate limitless number of symbols, the fountain codes are also termed "rateless codes" [9].

Luby Transform (LT) codes are the first class of practical fountain codes presented in [90]. Based on the exclusive or operation, the LT encoder can generate encoded symbols using a degree distribution termed robust soliton distribution [90]. Belief-propagation decoder is used to recover the source data based on exclusive or operation regardless of the order of the encoded symbols. Although LT codes have near-optimal performance, the computational complexity of the algorithms used are not linear in time [2]. A group of more advanced fountain codes, Raptor codes, were invented based on LT codes. As Fig. 3.2 depicts, the source symbols of a Raptor code are firstly encoded with a precode into a group of intermediate symbols with extra redundant symbols introduced. Then the intermediate symbols are encoded with an LT encoder to obtain the final encoded symbols. The decoder is then able to recover the source data at high probability with any subset of encoded symbols and small overheads [2]. By precoding the source symbols prior to an LT encoder, Raptor codes achieve an

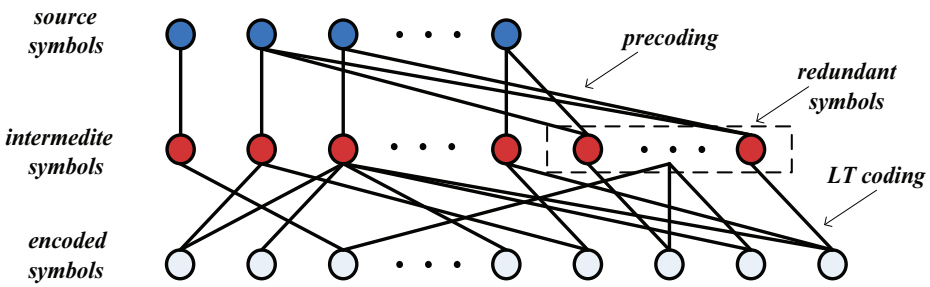

Figure 3.2: Demonstration of the Raptor Code Encoder Structure (figure based on Fig. 1 in [2])

encoding and decoding complexity to a constant factor [2]. One of the most successful versions of Raptor codes is Raptor 10 [61], which has been standardized by 3GPP for mobile cellular broadcast [91]. Raptor 10 code has also been studied and implemented in different channels such as Gaussian channels [92] and correlated Rayleigh channels [93]. In this work, Raptor 10 is employed to achieve adaptive data transmission rate when truncation occurs.

In the proposed fixed-scale system, although many modulation formats are possible, assume that the transmit image is formed by an array of pixels transmitting on-off keying (OOK) signals. For a given message, a Raptor 10 encoder emits a stream of packets which are mapped to individual pixels. The decoder can successfully recover the message packets once sufficient encoded packets are received, regardless of their order. In our design, each packet consists of one 32-bit encoding symbol identifier (ESI) to denote which encoded symbols are included and 8 encoded symbols. To determine whether the packet is received correctly, a 32-bit cyclic redundancy check code (CRC) is added at the end of each packet. Moreover, Raptor 10 codes are binary and systematic, i.e., for k source symbols, the first k encoded symbols are the same as the original message. Figure 3.3 presents the

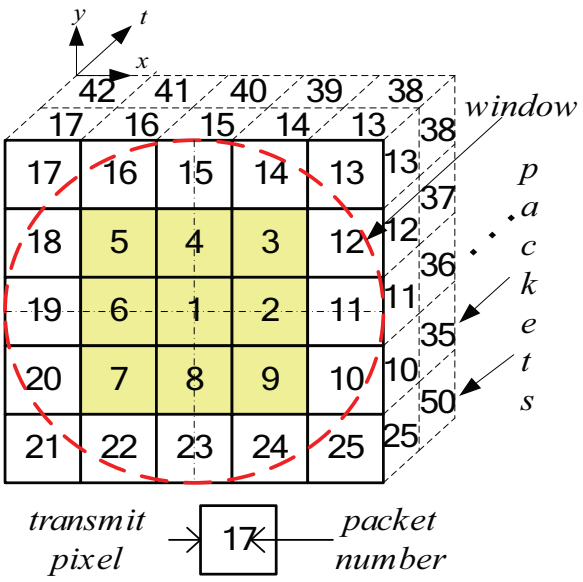

Figure 3.3: Mapping of Raptor 10 packets to the transmit image for fixed-scale MIMO system. Notice that systematic packets (highlighted packets) are placed near the optical axis under the assumption that orientation will be typically satisfied.

mapping of Raptor 10 packets to the array of transmit pixels in space and time for the fixed-scale MIMO system. In each time interval, individual pixels are assigned a packet to transmit via OOK. The systematic packets are mapped to points nearest the optical axis under the assumption that coarse alignment is likely performed. Notice that if the systematic packets are received, decoding can occur with little overhead [61]. In subsequent frame intervals, additional repair packets are transmitted by the transmit array. The Raptor 10 code allows the communication system to adapt to different ranges and orientations automatically. For example, as range is increased, the window size decreases and fewer sub-channels are received. In this case, the Raptor 10 code will require a longer time to collect sufficient packets, adapting the transmission rate to the channel conditions.

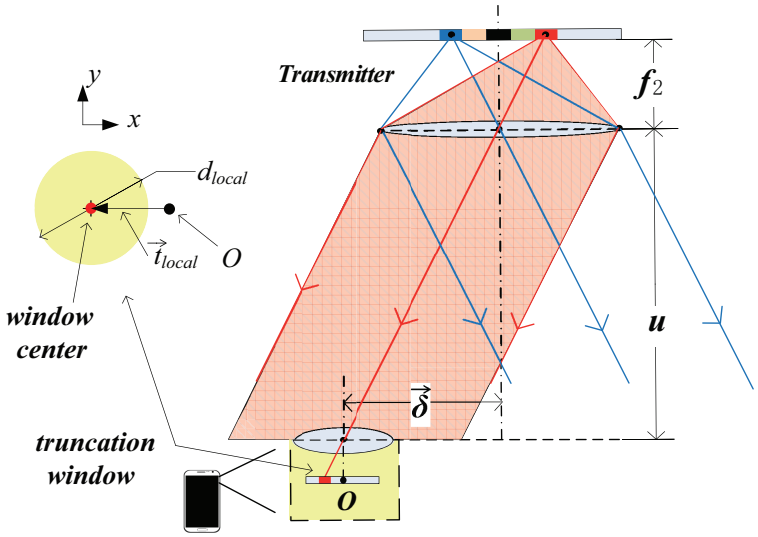

Figure 3.4: Localization Benefits

3.4 Localization Benefits

An extra benefit of this fixed-scale MIMO VLC design is that the spatial-angular mapping of the system can also provide localization benefits.

Assuming that the receiver has knowledge of the packet mapping at the transmitter, the relative location of each received packet stream can be identified (e.g., using the encoding symbol identifier (ESI) of the Raptor 10 packet [61]). That is, the transmitter can provide accurate angular information about its position to the receiver. This information could be used to refine alignment or to provide location and context specific data to the user. Similar concepts were also presented in [44] and [94], however, not in the context of using existing coding overhead to help in localization. Thus, this fixed-scale MIMO VLC design provides a hybrid localization and communication system.

In the special case as Section 2.3.3 discussed, where the transmitter and the receiver are parallel, a simpler approach is available. When $\theta = 0$ or it is negligibly

small, Fig. 3.4 illustrates this simple localization process. In this case, the origin of RCS O is merely the intersection point of the optical axis and the image sensor of the camera. Assuming the transmit image is infinite and all-white, by examining the truncation window on the receiver, the user can estimate the window diameter and the vector pointing from the RCS origin O to the center of the truncation window with various computer vision methods. d_{local} and $\vec{t}_{local}$ are used to denote these two measured parameters. Based on (2.9) and (2.10) in Section 2.3.3, a set of relations can be written as:

$$\begin{aligned} d_{local} &= \frac{f_2(l_t + l_r)}{u} \\ |\vec{t}_{local}| &= \frac{f_2|\vec{\delta}|}{u}. \end{aligned} \tag{3.3}$$

With know lens parameters f_1, f_2, l_t, l_r, the values of $|\delta|$ and u can be computed. Extra directional information can be further calculated based on $\vec{t}_{local}$. Then the exact location of the user relative to the optical center of the transmit lens is known. Such method does not need any specific information from the transmitter. In the simplest case, one transmit image is sufficient for retrieving location information. This is very attractive when only illumination is available from the transmitter and cheaper Fresnel lens can be used in this case. Although the transmit images are assumed to be all-white in this approach, coded images can also be used to estimate the truncation window parameters. General model in Section 2.3 also shows robustness with small tilting and translation. Further potential can be explored in the near future.

3.5 Conclusion

In this chapter, different components of the fixed-scale pixelated MIMO VLC system are compared based on their performances and costs. A guide on parameter selection is also provided to maximize the data rate while ensuring spatial synchronization of the system. To demonstrate the whole design process, two rough examples are given as references. Although the example based on μLEDs is shown to have superior performance over the one using LCD, the potential implementation cost will limit the use of advanced components such as μLED arrays. Therefore, when designing the system, the designer should balance between the system performance and cost to implement an affordable system with a moderate data rate. To further compromise the effect of the truncation described in Chapter 2, a rateless code, Raptor 10, is introduced to track channel erasure and achieve an adaptive data transmission speed at different working distances. Since Raptor 10 is a systematic version of rateless codes, the systematic packets are arranged near the optical axis where coarse alignment is performed for higher data throughput. Based on the theoretical analysis in Section 2.2, potential localization benefits of such design are also explored. By computing parameters of the truncation window, the receiver can locate itself in regard to the transmitter without a complicated calibration process. Following the design example in Section 3.2, Chapter 4 will build a proof-of-concept system to validate the channel model and this system design process.

Chapter 4

Experimental System and Measurement Results

In this chapter, a proof-of-concept experimental system is built to verify the fixed-scale pixelated MIMO VLC system proposed in this thesis. Based on this setup, both channel model and communication performance are recorded and examined in various situations. The magnification of the system is shown to be approximately fixed and the measurements of the truncation window also obey the model presented in Chapter 2. Throughput of the system is also tested using Raptor 10 code and compared with the theoretical estimation. The throughput of the system is shown to be adaptive to different truncation window sizes and performance with translation is also recorded. What is worth noticing is the experimental system is not optimized to achieve ideal communication performance. Based on the components available, this setup focuses mainly on demonstrating the idea of this new design.

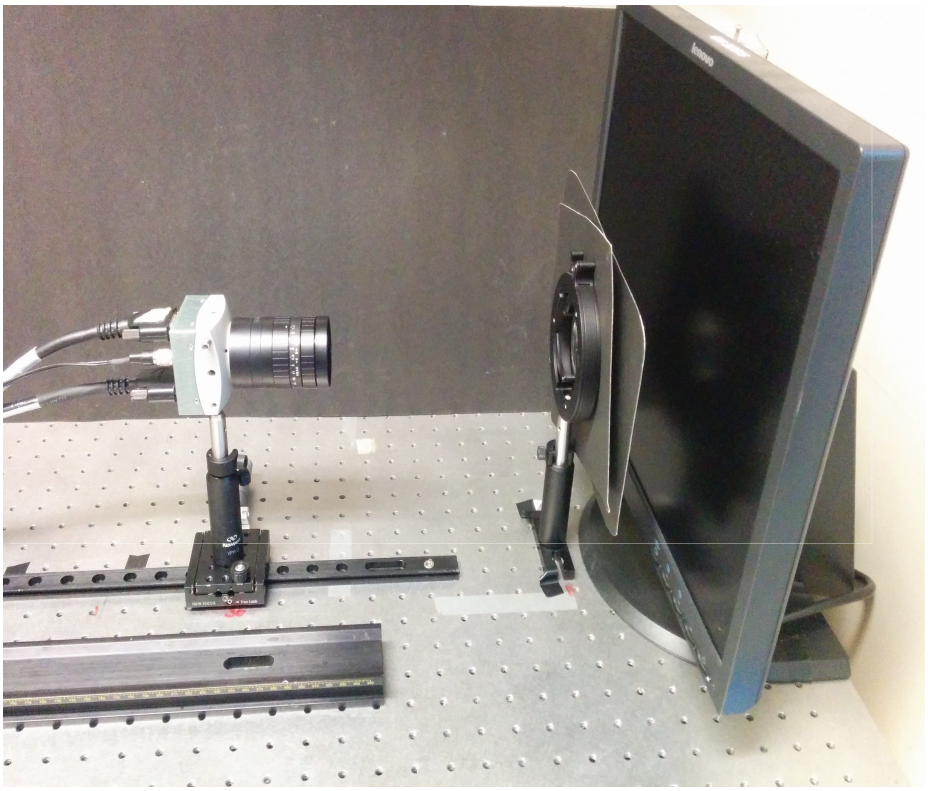

Figure 4.1: Experimental Setup of the Fixed-scale Pixelated MIMO System

4.1 Experimental Setup and Parameters

Figure. 4.1 presents a photograph of the experimental setup with parameters listed in Table 4.1.

The transmitter of this experimental system is chosen as an LCD display [95] with a resolution of 1280×1024 pixels. Although an OLED display can also serve as an

Table 4.1: Experimental Parameters

LCD pixel pitch D_t (mm)	0.294	LCD intensity (cd/m^2)	250
focal length f_1 (mm)	50	lens aperture l_t (mm)	50
focal length f_2 (mm)	25	camera aperture l_r (mm)	17.9
camera pixel size D_r (μm)	12	exposure time (ms)	10

alternative choice with larger viewing angle according to Section 3.1, this LCD display is sufficient when all tests are conducted with smaller translations within 5 mm and separation distances over 300 mm in our experiments. Raptor 10 coded OOK images are displayed and refreshed at the center of the display. All transmitted images were limited in size to 100×100 pixels. A coated double convex lens is placed at its focal length 50 mm from the display to perform space-to-angle mapping. The receiver is a CMOS camera [96] with a commercial lens [97] focused at infinity. With a fixed focal length 25 mm, the largest f-number 1.4 of the camera lens is chosen to maximize the lens aperture. The camera is installed onto a single rail and the centers of the transmit and receive lenses are controlled. The off-axis tolerance, $|\vec{\delta}|$, was limited to 10 mm while $\theta = 0$ in the experiment. All tests were done under nominal illumination levels. Although the components of the system may not be ideal for optimal communication performance, this experimental setup can still be a good proof-of-concept system with reasonable parameters selected according to Chapter 3 and all tests in the following sections are based on this setup.

4.2 Channel Measurements

In this section, channel measurements are done to verify the model presented in Chapter 2. Magnification and window diameters in different situations are tested and compared. Window gain and truncation effects are also examined with different examples. The theoretical model is shown to be able to predict the corresponding measurements correctly in different cases.

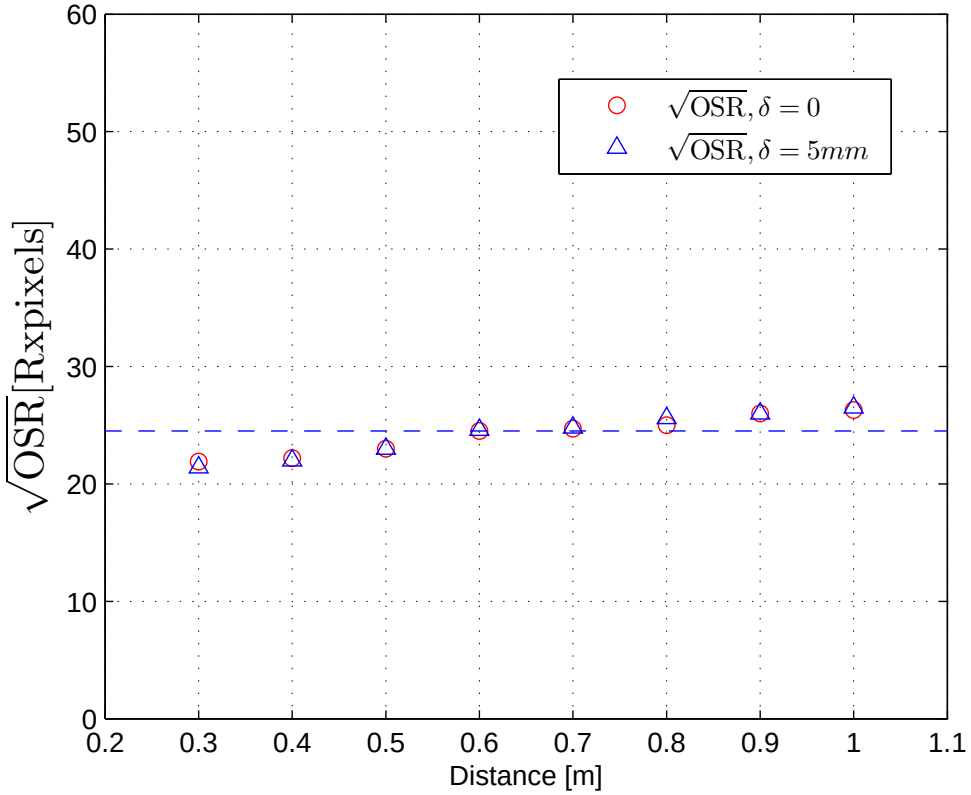

Figure 4.2: Magnification under Different Translations

4.2.1 Magnification

As stated in Chapter 2, magnification M is the key parameter in the pixelated MIMO VLC system. As (2.4) indicates, the theoretical magnification of the experimental setup is calculated as $M = \frac{f_2}{f_1} = 0.5$. Combined with D_t and D_r, the corresponding OSR can be computed with (3.1). Since all the pixels are modeled as square in shape, $\sqrt{\text{OSR}}$ can then be used as a metric of the magnification. This parameter can be interpreted as the side length of each transmit sub-channel in units of the number of receive pixels in the receive image. Notice that there is a constant scaling factor of 2 in all $\sqrt{\text{OSR}}$ in our measurements. This is due to the camera digitizer and can

be corrected with proper calibration at the receiver side. Considering all the factors stated above, the theoretical $\sqrt{\text{OSR}}$ is computed to be 24.5 in our system.

Quantitative measurements of $\sqrt{\text{OSR}}$ are depicted in Fig. 4.2. The $\sqrt{\text{OSR}}$ in Fig. 4.2 are all measured using edge detection method. The transmit image used is a square image, the size may vary from 10×10 to 3×3 at different distances to avoid truncation of the transmit images based on the theoretical truncation window diameter. The corresponding receive image is firstly processed with a Canny edge detector [98] to determine the edges of the transmit image. The Canny edge detection is a three step method based on gradients. The receive image is firstly smoothed with a Gaussian filter of variance 2 in order to alleviate noise in the image. The filtered image is then processed with a Sobel operator [99] to compute the intensity gradients of the image along different directions. Finally two thresholds are used to determine the edges: high threshold is 70% of the highest gradients and the low threshold is 30% in our tests. Gradients higher than the high threshold is termed strong edges and kept as edges. Positions with gradients between the two thresholds are also determined as edges only when they have adjacent pixels as strong edges. The resulting enclosed image area are then computed and averaged with the number of sub-channels transmitted. The result is the corresponding OSR at a certain distance.

In Fig. 4.2, both the $\sqrt{\text{OSR}}$ with $|\vec{\delta}| = 0$ and $|\vec{\delta}| = 5mm$ are plotted. As can be seen, the measured $\sqrt{\text{OSR}}$ generally agrees with the theoretical prediction with deviations within 15%. When a translation of 5 mm occurs, the corresponding $\sqrt{\text{OSR}}$ also obeys the theoretical prediction and shows the same trends with the measurements with no translation. Notice that dimension of transmit sub-channel varies by about 3 pixels as the range changes by a factor of over 3 times (0.3 to

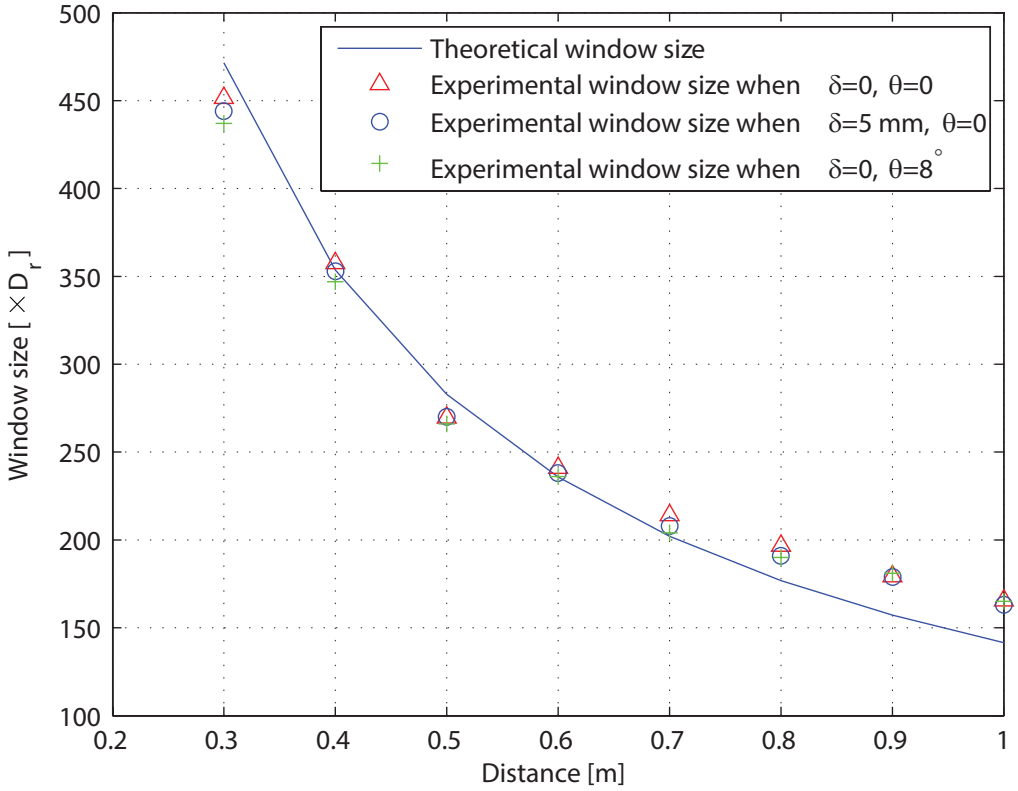

Figure 4.3: Window Diameter in Different Situations

1 m). Thus, the scale of each transmit sub-channel is nearly fixed at the receiver over a wide range of u.

4.2.2 Truncation Window

Quantitative measurements of the window diameter d is presented in Fig. 4.3. All measurements are performed for $|\vec{\delta}| = 0\ mm$ and $\theta = 0$, $|\vec{\delta}| = 5\ mm$ and $\theta = 0$ and $|\vec{\delta}| = 0$ and $\theta = 8°$. The window size is measured by transmitting an all white image and determining the edges of the received frame using a Canny edge detector similar to Section 4.2.1. The area of the enclosing figure is computed and the diameter of a

corresponding circle is plotted in the figure and compared to the model given in (2.9). For simplicity, all the diameters are expressed in the unit of receive pixel size D_r. Notice that there is good agreement for small u and the fit is looser at longer ranges. This is likely due to the fact that satisfying the paraxial approximation over longer ranges is more difficult and at longer ranges pixels are dimmer making measurement more difficult. Cases with different translations and tilting angles are also plotted. Notice that the curve of the diameters when $\theta = 0$ and $|\vec{\delta}| = 5\ mm$ appears to be identical to the case where neither translation nor tilting occurs. When $|\vec{\delta}| = 0$ and $\theta = 8°$, the diameters are shown to be less than the case without tilting, especially when u is smaller than 0.6 m. This can be explained by the diameter of window will be theoretically smaller according to (2.7). When distances is larger than 0.6 m, the diameter appears to be a tighter fit to the cases without tilting. This is likely due to the dimmer receive image which makes the edge detection harder and the smaller window diameter that makes the offsets negligible.

Fig. 4.4 shows the receive images when the transmit image is a cross in a checkerboard pattern. Images are taken for two ranges ($u = 400, 500$ mm) and for two off-axis translations ($|\vec{\delta}| = 0, 5$ mm). Additionally, the computed window size, following (2.9), is plotted as a red circle. The translation at different distances are computed with (2.10) and the corresponding window center is translated and plotted in the figure. Notice that the computed window diameter using ray optics is a good fit for the observed window size for different u. For a given range, changing $\vec{\delta}$ results in translation of the window center, thus truncating the transmit image at a different location. Most importantly, the magnification, i.e., size of each transmit pixel, does not change greatly by changing u. Changes in range result in changes in

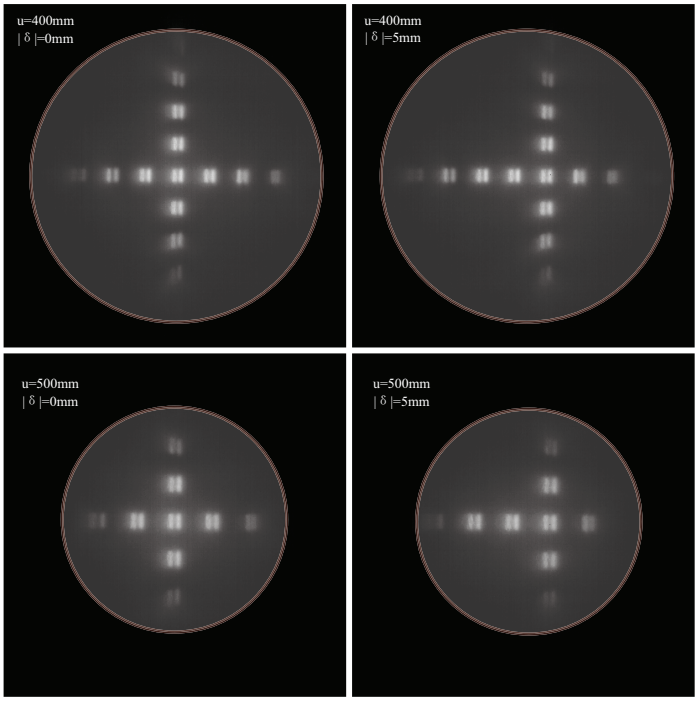

Figure 4.4: Comparison of Different Distances and Translations

the window diameter and the number of sub-channels available for communication.

The corresponding window gain is also plotted in Fig. 4.5, an all white image is sent and captured at 500 mm with the camera. The received image is then smoothed with an Gaussian filter to remove noise. The result of the filtered receive image is then normalized by its maximum value and plotted as a 2-dimensional function with the coordinates in units of D_r. A cross-sectional view is given to compare the plot with the theoretical predication. As can be seen in the figure, the measured gain obeys the example of window gain in Chapter 2. The gain near the window center can be considered constant with offsets less than 1%. The gain degrades quickly outside the central area of the window and is approximately symmetric to the center. What is worth noticing is that in some positions, the gain function does not totally agree with the theoretical predication, which should be symmetric and smooth. This is likely

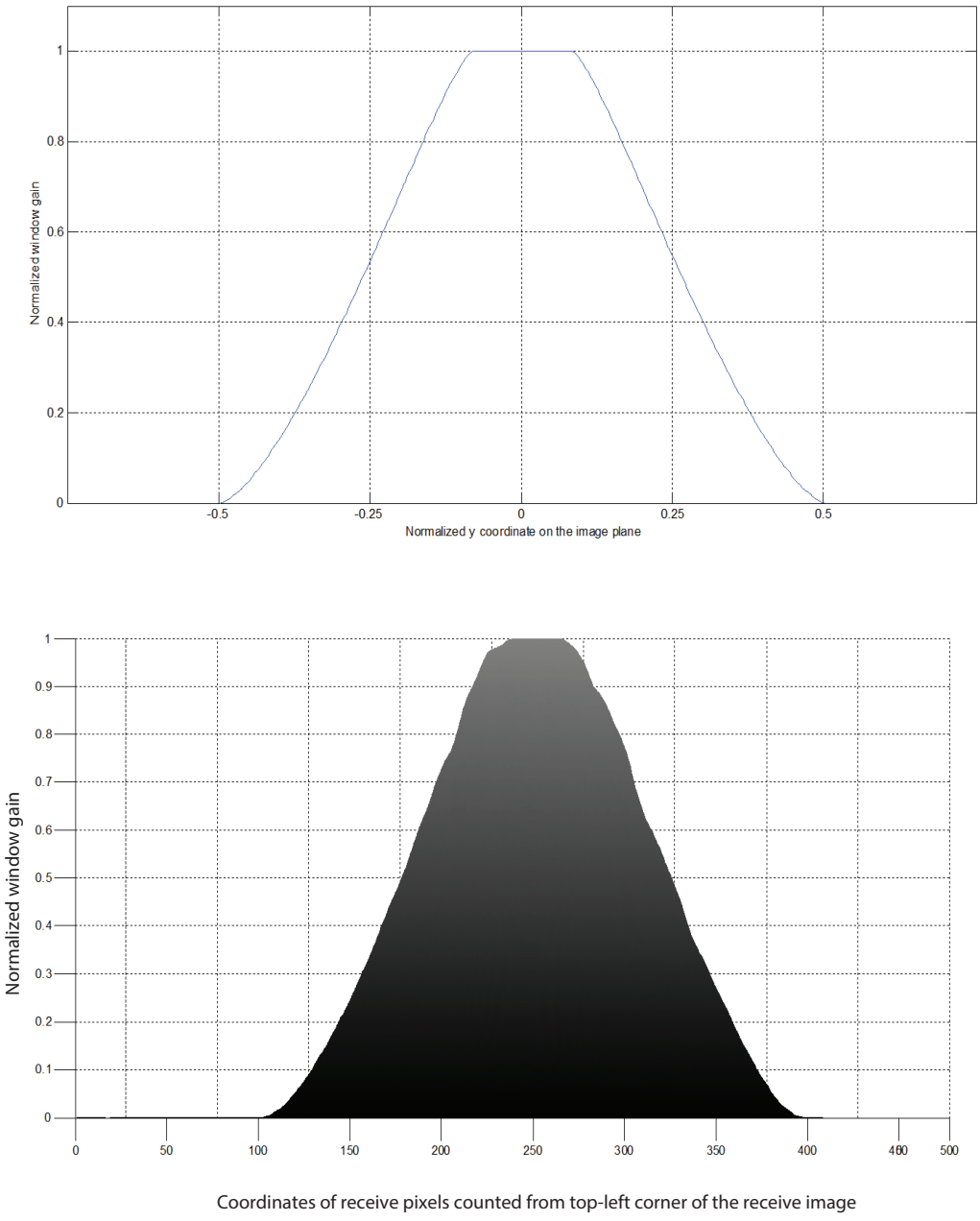

Figure 4.5: Comparison of Window Gains

due to the flawed surface of the lens and other optical distortions in the channel.

4.3 Rate Measurements

4.3.1 Information Rate

A small scale communication system was implemented to test the available data rates of the fixed-scale MIMO channel over different ranges. To estimate the performance limits of the system, assume that equiprobable on-off keying is transmitted on each transmit pixel. For each u, the signal-to-noise ratio (SNR) is measured for each transmit sub-channel at the receiver. The noise in the receive image is modeled as signal independent additive Gaussian noise with zero mean and is measured by sending and averaging 1000 illuminated images. The resulting noise standard deviation is found as $\sigma = 0.38$ in each receive pixel under nominal illumination levels. In each sub-channel, the overall signal power is measured and denoted as P_i. The corresponding SNR in each sub-channel are then computed as:

$$\mathrm{SNR_i} = \frac{P_i}{\sigma^2}. \tag{4.1}$$

The mutual information subject to binary equiprobable signalling, C_i, can then be computed for each transmit sub-channel visible in the window domain $\mathcal{W}$ at the receiver similar to the method described in [100]. For each SNR, 10000 times of Monte Carlo experiments are used to estimate the mutual information as C_i. Assuming no interference between the transmit sub-channels, the overall information rate of this channel can be estimated as $C = \sum C_i$ in units of bits per frame and is shown with the solid line in Fig. 4.6.

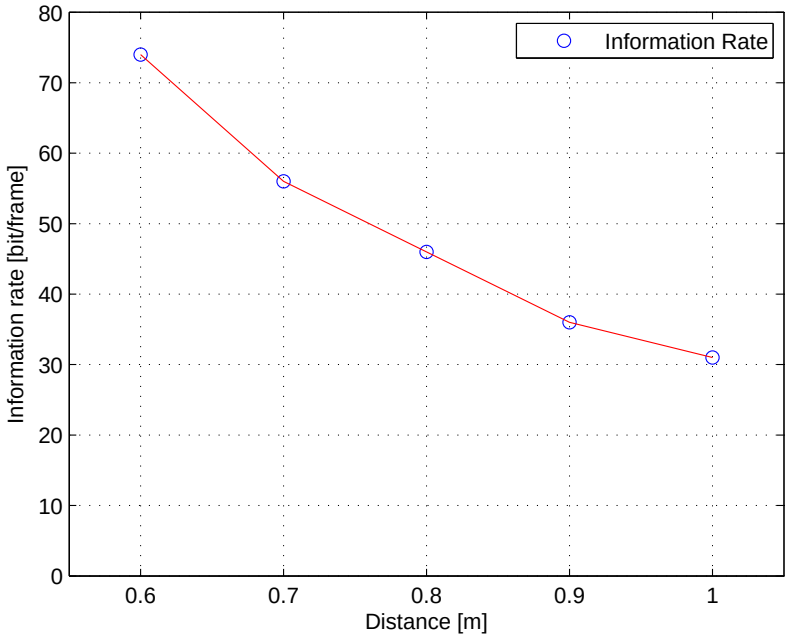

Figure 4.6: Information Rate

The theoretical information rate is shown to be a good fit of the window size presented in Fig. 4.3. This is due to the high SNR of most sub-channels received. However, this is just a rough approximation of the information rate of the channel because although the number of sub-channels can be calculated based on the window size and the magnification, the actual truncation of sub-channels may vary at different locations and distances. According to [40], with limited signal power, the overall information rate can be increased with more sub-channels with poor SNRs. So this information rate may change under different truncation situations. A more robust estimation can be done with more measurements to compensate for the variations in the number of visible sub-channels.

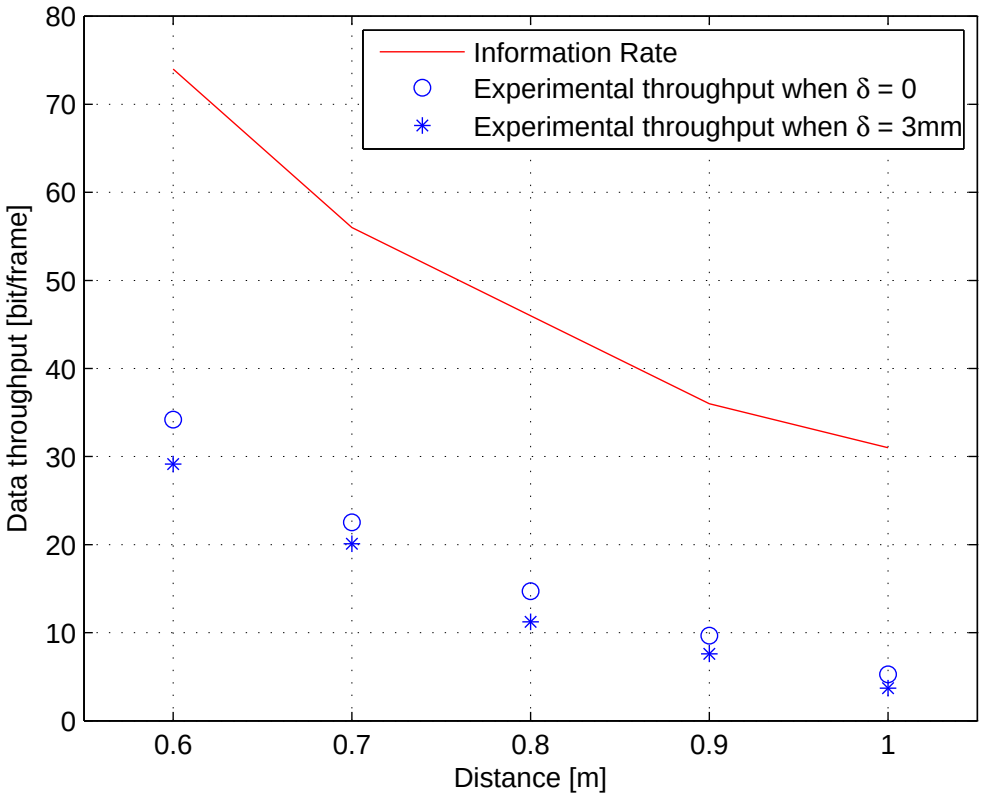

Figure 4.7: Data rates. The red solid curve indicates the maximum information rate subject to binary modulation of each transmit sub-channel over u. Realized data rates with Raptor 10 codes for $|\vec{\delta}| = 0, 3$ mm are also plotted.

4.3.2 Throughput

The throughput of the system is also plotted in bits/frame when a Raptor 10 code is applied to the transmit pixels for $|\vec{\delta}| = 0, 3$ mm and shown in Fig. 4.7. The Raptor 10 code is taken from the standard [61] with message length $k = 1024$ with a symbol size of 32 bits. The code used in this experiment is modified based on the code presented in [9]. Recall that the Raptor 10 code is systematic and the message packets are clustered in the middle of the transmit frame with repair symbols

surrounding as depicted in Fig. 3.3. At the receiver, pixels corresponding to each transmit sub-channel are summed and used as a metric for detection. As is typical in Raptor coded systems, a 32-bit cyclic redundancy check is appended to each transmitted packet to detect and discard any packets in error. The measured rates are averaged over at least 1000 frames to compute the throughput. Notice that there is a gap between the computed upper bound information rate and the Raptor 10 encoded system. Additionally, the Raptor code scales the throughput of the channel for different ranges automatically given the scaling of the window. Notice additionally that there is a small rate penalty when $\vec{\delta}$ is non-zero. This is due to fact that when $\vec{\delta} = 0$ decoder captures many of the systematic symbols sent by the encoder making decoding possible with less overhead. When off axis, the decoder must collect additional repair packets to construct with transmitted message resulting in an increased overhead. Qualitatively, the performance of the system depends greatly on the quality of lenses and camera used. For large values of $|\vec{\delta}|$ the rate may also adversely affected by aberrations in the receiver lens. However, the Raptor code is able to adapt the rate to provide useable rates over a variety of ranges and misalignments.

4.4 Comparison to Conventional MIMO Pixelated System

Notice that unlike the conventional pixelated MIMO system [40], this fixed-scale system is relatively robust to misalignments and does not require refocusing or knowledge of the range. In the fixed-scale system, the receiver lens is focused at

infinity and fixed for all ranges and data is multiplexed in angle and not in space directly.

The chief advantage of the fixed-scale MIMO system is that it provides a number of independent sub-channels from the transmitter to the receiver which decrease with range. Conversely, the conventional pixelated system, with only a single lens at the receiver, will have a larger field-of-view potentially capturing more transmit pixels, however, it is sensitive to focusing and scale errors.

Consider the example system design given in Section 3.2 based on a smartphone camera receiver and an array of μLEDs as the transmitter. It was estimated that the fixed-scale MIMO system would have on the order of 945 independent sub-channels at a range of 1 m. Consider a conventional pixelated MIMO system with the same smart phone camera ($f_2 = 4$ mm) imaging the array of μLEDs directly (i.e., without the transmit lens). For the same 1 m range, assuming that the camera is properly focused on the transmitter array, it can be found that approximately 156 transmit pixels are imaged onto each receive pixel. That is, the transmitter must have knowledge of the user position and orientation to coordinate the emitted signals from each μLED to convey data to receiver. Although the total number of available channels will depend on the field of view of the camera, significant complexity and channel knowledge are essential in order to extract any multiplexing gains.

Thus, the key advantage of the fixed-scale MIMO system is to provide a low complexity system which is robust to misalignment and provides multiplexing gains rather than maximizing the number of available spatial channels at the receiver.

4.5 Conclusion

In this chapter, a proof-of-concept experimental fixed-scale pixelated MIMO VLC system is built with available devices. Rather than aiming at high performance, the main purpose of this setup is to demonstrate and verify the idea of the design. Channel measurements from magnification to the window diameters are measured and compared to theoretical predications. The result is shown to obey the theoretical model with small offsets. The rate performance of the system is also tested. With Raptor 10 code built in, data throughput is recorded and compared with theoretical estimation of information rate. The throughput is found to degrade as the window shrinks with increasing separation distances between the transmitter and the receiver. Off-axis case is also examined to provide insight for packet allocation. Finally this setup is briefly compared with traditional system under similar circumstances. The design is shown to surpass the traditional one especially at larger distances with lower complexity.

Chapter 5

Conclusions and Future Directions

The work in this thesis focuses on the modeling and design of a fixed-scale MIMO visible light communication system for indoor short range data transmission.

Although MIMO optical systems are shown to be a promising option for short range wireless communication in Chapter 1, these traditional designs suffer from strict alignment requirements, perspective distortion and different magnifications at various links ranges. Although these problems can be solved by different techniques, the design of a system with low complexity remains challenging. By introducing an extra spatial-angular mapping, this thesis proposes a fixed-scale MIMO VLC system with fixed magnification and easy alignment at all working distances while ensuring reliable data transmission. Details of the modeling of this novel design is provided in Chapter 2 and robustness of this model is examined in different conditions as well. Due to the truncation of the transmit images, only a certain number of transmit pixels (sub-channels) are visible at the receiver. The number of visible sub-channels depends on the angular subtense of the receiver relative to the transmitter and a

communication model is provided in Chapter 2 to help calculated the visible sub-channels at different working distances accordingly. Chapter 3 further discusses the design process of a fixed-scale MIMO VLC system with a balance between cost and performance. A type of fountain code with linear encoding and decoding time (Raptor 10) is also introduced to automatically track the available rate depending on the number of sub-channels available at the receiver.

In Chapter 5, an experimental system is built to verify the theoretical analyses based on an LCD and a CMOS camera. The channel measurements and data rate are recorded and discussed in different conditions and the throughput of the system is shown to be adaptive to the truncation image sizes at various link distances. Throughput of around 10 bit/frame is observed at 0.9 m. This proof-of-concept system focuses on demonstration of the idea rather than superior performance, therefore, higher transmission rate can be achieved with high-definition components used. A simple comparison is made with the traditional system at last. The newly introduced system is shown to have superior performance especially working at longer distances.

The key advantage of this fixed-scale system is that the magnification of the receive image stays fixed at all link distances. Therefore, no range estimation is needed in order to determine the scale of the receive image. Moreover, neither exact focusing nor re-focusing is required to capture clear images with the receiver focusing at infinity. Consequently, a much simpler structure of the receiver can be sufficient to work reliably. Combined with rateless code, the system complexity is even lower with adaptive rates at different distances. These features are very attractive to indoor short range broadcasting system designed for multiple users with simple receivers.

Benefiting from the spatial-angular mapping, each user of this system is able to receive real time data on the move and the receivers need little adjustments when located at different positions. Extra localization benefits can also be included to build a multi-purpose hybrid system. Considering the development of μLEDs arrays and high-definition image sensors, the fixed-scale pixelated MIMO system is a promising choice for visible light communication systems in the near future.

5.1 Future Work

This work focuses on the modeling and the demonstration of the fixed-scale pixelated MIMO visible light communication system. Although the model and performance are measured and verified in Chapter 4, the throughput of the system is still not ideal for practical use. Apart from employing high-end components in the system, several structural improvements can also be made to achieve higher data rate. In general, there are three directions of extensions that can be explored in the future.

The first one is the simulation and experiments for fixed-scale MIMO systems with higher order modulation. In the system proposed in this thesis, only OOK modulation is discussed. According to [100], higher order of modulation shows better transmission performance by exploiting more degrees of freedom. With a camera receiver that can offer good imaging sensitivity, the performance of the system can be improved with more sophisticated modulation schemes. However, quantization noise may be a significant issue in such designs.

The use of multiple color emitters and receiver elements can also be investigated. Based on only black and white images, the proposed system in fact assigning same data to multi-colour sub-pixels in the transmitter. Consisting of three colour strips,

the sub-pixels in each LCD pixel can be independently addressed to introduce extra degrees of freedom. Although the rate of the multi-color system is predicted to be higher than the work in this thesis, the degree of freedom in each colour mode decreases and the separation between different signal frequencies may become a main interest then.

Additionally, the design of more efficient rateless codes to track channel variations is essential to maximize the achievable rates of fixed-scale MIMO systems. As a powerful extension of the Raptor 10 code, RaptorQ code embraces many improvements such as supporting larger source block, better overhead-failure curve and exceptional computation complexities [9]. The challenge of implementation of a RaptorQ code mainly lies in the decoders. With proper hardware selected, a high speed communication link can be designed.

Lastly, as mentioned in Section 3.4, a hybrid system that combines localization, data transmission and illumination can be built to fully utilize the existing visible light sources in the infrastructure. The use of Fresnel lens in such system can also be investigated. The link speed may be impaired by the poor imaging quality of Fresnel lens, however, the low cost of such lenses with large physical dimensions may still be worth the effort of study.

Appendix A

Calculation of Window Diameter

In the appendix, notations similar to Chapter 2 is used to derive the window parameters. The notation with capital letter $K(x, y)$ is used to represent a point and its corresponding coordinates. The notation with lowercase letter $w(x, y)$ is used to denote a 2-dimensional function with x, y as variables. AB represents a segment and $|AB|$ is its corresponding length. S is used to denote the area of a certain 2-dimensional domain and $\overset{\frown}{ABC}$ is the arc where points A, B, C lie in.

In Chapter 2, a guideline is provided to calculate the diameter of the truncation window $\mathcal{W}$. All points in this guideline are represented with coordinates in the TCS described in Chapter 2. To demonstrate the detailed calculation process clearly with simpler notations, a temporary coordinate system is defined in Appendix A and Appendix B to determine window parameters. In Fig. A.1, this temporary coordinate system is depicted. With the origin at the optical center of the transmit lens and the optical axis as x-axis, the corresponding coordinates of the points can be computed as:

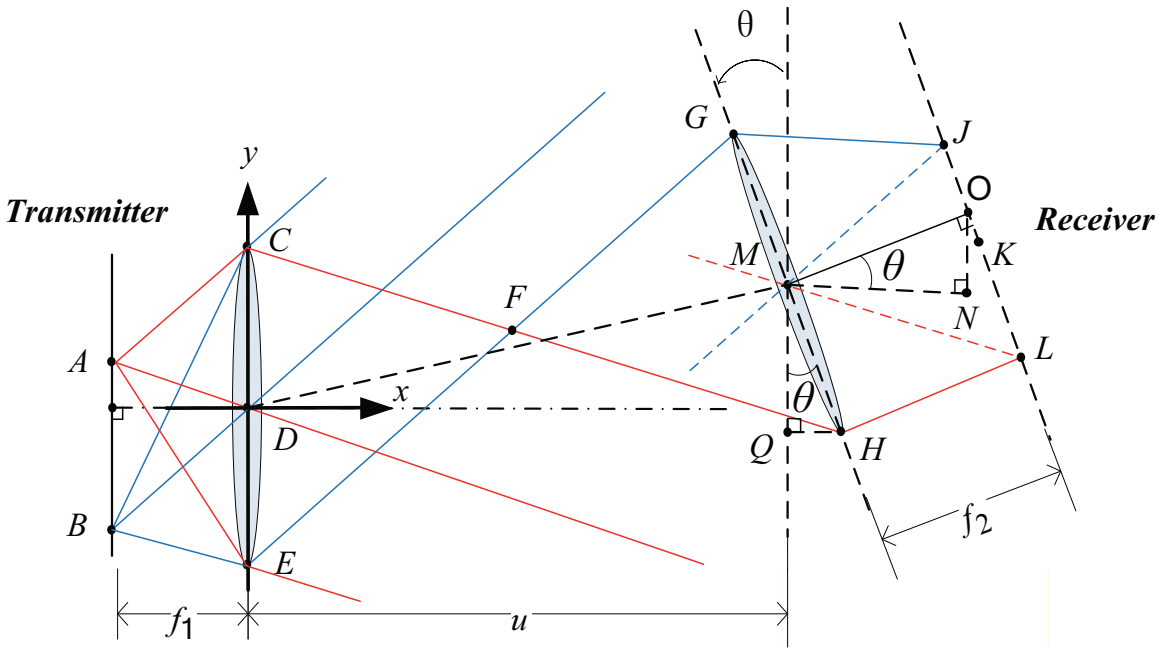

Figure A.1: Calculation of Window Parameters with Temporary Coordinates

$$
\begin{aligned}
&C(0, \frac{l_t}{2}), D(0, -\frac{l_t}{2}), M(u, |\vec{\delta}|) \\
&G(u - \frac{l_r \sin\theta}{2}, |\vec{\delta}| + \frac{l_r \cos\theta}{2}) \\
&H(u + \frac{l_r \sin\theta}{2}, |\vec{\delta}| - \frac{l_r \cos\theta}{2}) \\
&O(u + f_2 \cos\theta, |\vec{\delta}| + f_2 \sin\theta).
\end{aligned} \tag{A.1}
$$

The coordinates of point H is calculated based on right triangle $\triangle MQH$. With known length of $|MQ| = \frac{l_r}{2}$ and θ, we have $|HQ| = \frac{l_r \sin\theta}{2}$ and $|MQ| = \frac{l_r \cos\theta}{2}$. Coordinates of point M are straightforward: $M(u, |\vec{\delta}|)$. Therefore, coordinates of point H can be computed in regard to point M as $(u + \frac{l_r \sin\theta}{2}, |\vec{\delta}| - \frac{l_r \cos\theta}{2})$. Analogously, coordinates of point G can be calculated.

The coordinates of point O is calculated based on right triangle $\triangle MON$. With

known length of $|MO| = f_2$ and θ, we have $|MN| = f_2 \cos\theta$ and $|NO| = f_2 \sin\theta$. Coordinates of point O can be computed in regard to point M as $(u + f_2 \cos\theta, |\vec{\delta}| + f_2 \sin\theta)$.

As Chapter 2 described in Fig. 2.6, the diameter of the circular domain $\mathcal{W}$ is shown to be $d = |JL|$. Following the guideline in Chapter 2, the diameter can be calculated step by step.

The equations of the lines which CH, EG lie in can be expressed as:

$$\begin{aligned} EG: \ y &= \frac{0.5l_r \cos\theta + |\vec{\delta}| + 0.5l_t}{u - 0.5l_r \sin\theta} x - 0.5l_t \\ CH: \ y &= \frac{-0.5l_r \cos\theta + |\vec{\delta}| - 0.5l_t}{u + 0.5l_r \sin\theta} x + 0.5l_t. \end{aligned} \tag{A.2}$$

The coordinates of intersection point of the two lines, F, is found as:

$$F(x_F, y_F) = \left(\frac{l_t(u^2 - 0.25l_r^2 \sin^2\theta)}{ul_r \cos\theta + ul_t + |\vec{\delta}| l_r \sin\theta}, \frac{u|\vec{\delta}|l_t + 0.25l_t l_r^2 \sin\theta\cos\theta + 0.25l_t^2 l_r \sin\theta}{ul_r \cos\theta + ul_t + |\vec{\delta}| l_r \sin\theta}\right).$$

Note that $\triangle FCE \sim \triangle DAB$, giving $x_F/f_1 = l_t/|AB|$.

Combining with (2.4), the diameter of the domain $\mathcal{W}$ is determined to be:

$$d = \frac{f_2(ul_r \cos\theta + ul_t + |\vec{\delta}| l_r \sin\theta)}{u^2 - \frac{l_r^2 \sin^2\theta}{4}} \tag{A.3}$$

where $\theta \in [0, \pi/2)$ and $u > l_r/2$.

Appendix B

Calculation of Window Center

Using the same Fig. A.1 and temporary coordinates, the center of the circular domain $\mathcal{W}$ is defined as $K(0, y_p)$ in the RCS. In the general case described in Fig. 2.6, the center of the window can be found as $K(0, -|OK|)$. Since the diameter of $\mathcal{W}$ is already computed in (A.3), we have $|OK| = |JK| - |JO| = 0.5d - |JO|$.

Using parallel relations $EG \parallel MJ, GH \parallel JK$ and known coordinates of points M, O, the lines which MJ, JK lie in can be found as:

$$\begin{aligned} MJ:\ y &= \frac{0.5l_r\cos\theta + |\vec{\delta}| + 0.5l_t}{u - 0.5l_r\sin\theta}x - \frac{0.5|\vec{\delta}|l_r\sin\theta + 0.5ul_r\cos\theta + 0.5ul_t}{u - 0.5l_r\sin\theta} \\ JK:\ y &= \frac{-\cos\theta}{l_r\sin\theta}x + |\vec{\delta}| + f_2\sin\theta + \frac{u\cos\theta}{l_r\sin\theta} + \frac{f_2\cos^2\theta}{l_r\sin\theta}. \end{aligned} \tag{B.4}$$

The intersection point of the two lines J is derived as

$$
\begin{aligned}
J((&2u^2\cos\theta - l_r f_2 \sin^3\theta + 2uf_2\cos^2\theta - ul_r\sin\theta\cos\theta + 2|\vec{\delta}|ul_r\sin\theta \\
&+ ul_t l_r\sin\theta - l_r f_2\sin\theta\cos^2\theta + ul_r^2\sin\theta\cos\theta + 2ul_r f_2\sin^2\theta) \\
&(2u\cos\theta + l_r^2\sin\theta\cos\theta - l_r\sin\theta\cos\theta + 2l_r|\vec{\delta}|\sin\theta + l_t l_r\sin\theta)^{-1}, \\
&(l_r f_2\cos^3\theta + 2|\vec{\delta}|f_2\cos^2\theta + l_t f_2\cos^2\theta + |\vec{\delta}|l_r^2\sin\theta\cos\theta \\
&- |\vec{\delta}|l_r\sin\theta\cos\theta + 2u|\vec{\delta}|\cos\theta + l_r^2 f_2\sin\theta\cos\theta + 2|\vec{\delta}|^2 l_r\sin\theta \\
&+ 2|\vec{\delta}|l_r f_2\sin^2\theta + |\vec{\delta}|l_t l_r\sin\theta + l_t l_r f_2\sin^2\theta)(2u\cos\theta \\
&+ l_r^2\sin\theta\cos\theta - l_r\sin\theta\cos\theta + 2|\vec{\delta}|l_r\sin\theta + l_t l_r\sin\theta)^{-1}).
\end{aligned}
\tag{B.5}
$$

Noticing that $|JK| = 0.5d$, $|OK| = |JK| - |JO|$ can be calculated as the absolute value of the y component $|y_p|$. Thus, by adjusting the sign, the window center can be found as $(0, y_p)$, where

$$
\begin{aligned}
y_p = &- \frac{f_2(ul_t + |\vec{\delta}|l_r\sin\theta + ul_r\cos\theta)}{2(u^2 - \frac{l_r^2\sin^2\theta}{4})} + ((|\vec{\delta}| + f_2\sin\theta(l_r f_2\cos^3 + 2|\vec{\delta}|f_2\cos^2\theta \\
&+ f_2 l_t\cos^2\theta + |\vec{\delta}|l_r^2\sin\theta\cos\theta - |\vec{\delta}|l_r\sin\theta\cos\theta + 2u|\vec{\delta}|\cos\theta + l_r^2 f_2\sin^2\theta\cos\theta \\
&+ 2|\vec{\delta}|^2 l_r\sin\theta + 2|\vec{\delta}|l_r f_2\sin^2\theta + |\vec{\delta}|l_t l_r\sin\theta + l_t l_r f_2\sin^2\theta)(2u\cos\theta + l_r^2\sin\theta\cos\theta \\
&- l_r\sin\theta\cos\theta + 2|\vec{\delta}|l_r\sin\theta + l_t l_r\sin\theta)^{-1})^2 + (u + f_2\cos\theta - (2u^2\cos\theta \\
&- l_r^2 f_2\sin^3\theta + 2uf_2\cos^2\theta - ul_r\sin\theta\cos\theta + 2|\vec{\delta}|ul_r\sin\theta + ul_t l_r\sin\theta \\
&- l_r f_2\sin\theta\cos^2\theta + ul_r^2\sin\theta\cos\theta + 2ul_r f_2\sin^2\theta)(2u\cos\theta + l_r^2\sin\theta\cos\theta \\
&- l_r\sin\theta\cos\theta + 2|\vec{\delta}|l_r\sin\theta + l_t l_r\sin\theta)^{-1})^2)^{\frac{1}{2}}.
\end{aligned}
\tag{B.6}
$$

Noting that in the coordinates of point G, H in Fig. A.1, if θ is significantly small,

$\sin\theta \approx \theta \approx 0, \cos\theta \approx 1$, therefore the point G, H can be approximated by:

$$G(u, |\vec{\delta}| + \frac{l_r}{2}), H(u, |\vec{\delta}| - \frac{l_r}{2}).$$

Especially when θ is considerably small, point F in Fig. A.1 approaches line DM formed by the two optical centers. The equation for DM is:

$$DM: \ y = \frac{|\vec{\delta}|}{u}x. \tag{B.7}$$

Applying x_F, the x component of point F, to this line equation, we have the corresponding y component value to be: $\frac{u|\vec{\delta}|l_t - 0.25|\vec{\delta}|l_t l_r^2 \sin^2\theta/u}{ul_r\cos\theta + ul_t + |\vec{\delta}|l_r\sin\theta}$.

When θ is small, the first term dominates in the coordinate above and it can be approximated as y_F of point F. Therefore, point F can be considered to approach the line DM. The window center can thus be approximated by combining the special case and the tilting translation as $(0, y_p)$, where $y_p \approx \frac{f_2|\vec{\delta}|}{u} - f_2\tan\theta$.

Appendix C

Computation of Window Gain

One example of the computation of the window gain $w(x, y)$ described in Section 2.3.4 is given within the domain $\mathcal{W}$.

As Section 2.3.4 discussed, the window gain is primarily determined by the number of ray bundles received at a particular angle. Before computing the window gain, several important assumptions are made.

Firstly, each transmit pixel emits intensity isotropically. Therefore, in Fig. 2.1, any pixel in the transmit image will contribute the same amount of power when arrives at the collimating lens. In practice, this may not necessarily be valid since the spatial distribution of the transmit pixel power largely depends on the transmitter type. However, if the transmit image is considerably small in regard to the transmit lens, the intensity distribution of each pixel can be approximated as identical distribution.

Secondly, light transmitted from a given transmit pixel is assumed to leave the collimating lens as a cylindrical beam with a uniform power distribution. Again, this condition may not hold considering different lenses and transmitters used.

The intersection of a portion of the cylindrical transmit beam by the receive lens

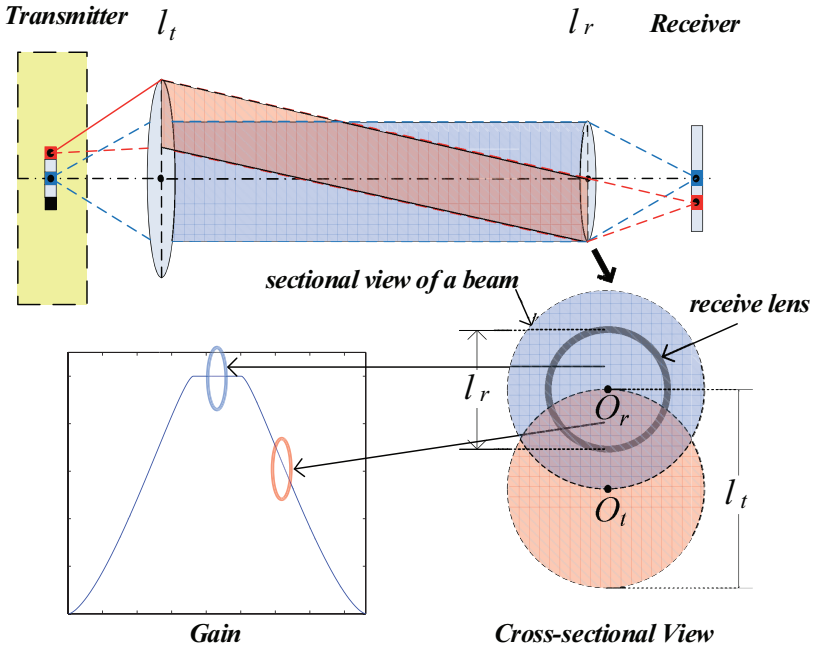

Figure C.2: Detailed Calculation Process of Window Gain

results in a variation of gain over the domain for $w(x, y)$, which can be found by ray tracing.

As a rough example, considering the case where $l_t > l_r$ and $|\delta = 0|, \theta = 0$, Fig. C.2 is repeated from Chapter 2 for convenience, which shows the gain calculation process. Due to the symmetry of the system, only the window gain on one diameter of the circular domain $\mathcal{W}$ is computed: $w(0, y)$.

First of all, take a cross-sectional view of the system on the plane formed by the receive lens. As discussed previously, the cylindrical beams formed by each transmit pixel is intersected as a circle that has exactly the same diameter as the transmit lens. Due to different positions of the transmit pixels, the cylindrical beams are inclined at different angles to the optical axis of the transmit lens. Consequently, in the cross-sectional view, such phenomenon is described by the different separation

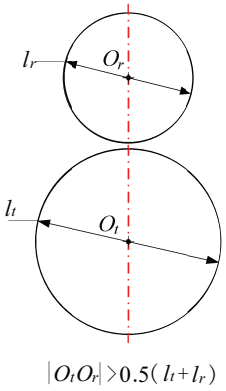

Figure C.3: Calculation of Window Gain (Case I)

distance between the centers of the two circles formed by the receive lens and circular sectional region of each transmit pixel.

Next, based on our assumptions, different intersection areas at different separating distances of the two circles simply indicate different amount of optical power accumulated on the sensor of the receiver. The corresponding image point of each transmit pixel is then obtaining different gains in the truncation window.

In Fig. C.3, one case of the intersection is shown with the proposed parameters. O_r represents the center of the receive lens while O_t stands for the center of the sectional circular region for a beam from a transmit pixel. As illustrated in Fig. C.3, when the separation distance is large enough, the intersection area of the two circles S is 0. This indicates any light from the corresponding transmit pixel is not captured by the receiver, thus the pixel is truncated by the window.

When the separation distance $0.5(l_t + l_r) > |O_tO_r| > 0.5\sqrt{l_t^2 + l_r^2}$, the intersection of the circles is shown in Fig. C.4. To compute the area of intersection, area formed by $\widehat{ADC}$ and string AC is firstly calculated as S_1. Area formed by $\widehat{AEC}$ and string AC can be denoted as S_2. The total intersection area S is then calculated as $S = S_1 + S_2$.

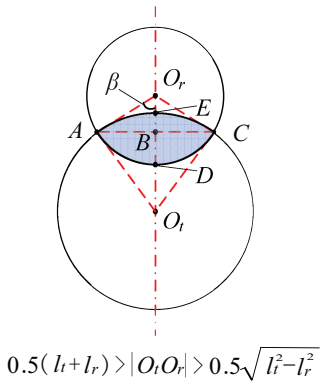

Figure C.4: Calculation of Window Gain (Case II)

Denote the area of sector AO_rC as S_{AO_rC} which includes the shaded area in the figure and the area of triangle $\triangle AO_rC$ as $S_{\triangle AO_rC}$, S_1 can be found as:

$$S_1 = S_{AO_rC} - S_{\triangle AO_rC}. \tag{C.8}$$

In $\triangle AO_rO_t$, using law of cosines, the cosine value of β can be obtained as:

$$\cos\beta = \frac{|AO_r|^2 + |O_tO_r|^2 - |AO_t|^2}{2|AO_r||O_tO_r|} = \frac{(0.5l_r)^2 + |O_tO_r|^2 - (0.5l_t)^2}{l_r|O_tO_r|}. \tag{C.9}$$

Therefore, the area of $\triangle AO_rC$ is written as:

$$S_{\triangle AO_rC} = 0.5\sin 2\beta |AO_r||CO_r|. \tag{C.10}$$

Moreover, the area of sector AO_rC is computed as:

$$S_{AO_rC} = \frac{\sin 2\beta}{2\pi}\pi|AO_r|^2. \tag{C.11}$$

Area S_1 can then be obtained with (C.8).

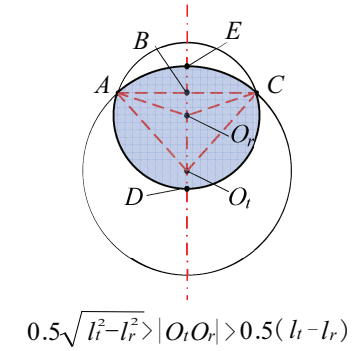

Figure C.5: Calculation of Window Gain (Case III)

Similarly, area formed by $\widehat{AEC}$ and string AC can be calculated as S_2 with previous steps. Consequently, the total intersectional area in Fig. C.4 is determined with $S = S_1 + S_2$.

When the separation distance $0 \leq |O_tO_r| \leq 0.5\sqrt{l_t^2 + l_r^2}$, the calculation is slightly different. The area S_2 formed by $\widehat{AEC}$ and string AC is firstly calculated in Fig. C.5 in a similar way as Fig. C.4.

Then area S_1 formed by $\widehat{ADC}$ and string AC is calculated in Fig. C.5 differently. Denote the area of sector AO_rC as S_{AO_rC} which includes the shaded area and area of triangle $\triangle AO_rC$ as $S_{\triangle AO_rC}$, S_1 can be found as:

$$S_1 = S_{AO_rC} + S_{\triangle AO_rC}. \tag{C.12}$$

The overall area is then computed as: $S = S_1 + S_2$.

When the separation distance satisfies $0 < |O_tO_r| < 0.5(l_t - l_r)$, the intersection area stays the same as Fig. C.6 indicates.

Due to the symmetry of the gain relative to the receive lens center O_r, the other half of the gain function can be computed correspondingly. The only adjustments needed is the change of the signs.

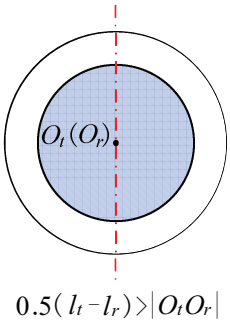

Figure C.6: Calculation of Window Gain (Case IV)

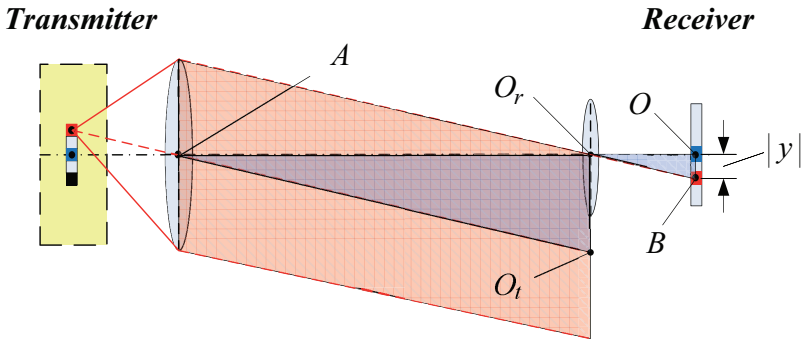

Figure C.7: Relation Between $|y|$ and $|O_tO_r|$

Notice that the gain function is using $|O_tO_r|$ as the variable. To denote the gain with RCS coordinate, Fig. C.7 shows the relation between different $|O_tO_r|$ and the absolute value of y component of the corresponding image point. Notice that $\triangle AO_rO_t \sim \triangle O_rOB$, we have:

$$|y| = \frac{f_2|O_tO_r|}{|AO_r|}. \tag{C.13}$$

Therefore, by replacing $|O_tO_r|$ with $|y|$ and adjusting the signs, the same result as (2.11) can be obtained.

Bibliography

[1] "Generate barcodes online," http://barcode.tec-it.com/en, accessed: 2016-02-21.

[2] A. Shokrollahi, "Raptor codes," *IEEE Transactions on Information Theory*, vol. 52, no. 6, pp. 2551–2567, 2006.

[3] Cisco, "Cisco visual networking index: Global mobile data traffic forecast update, 2016 to 2021 white paper," http://www.cisco.com/c/en/us/solutions/collateral/service-provider/visual-networking-index-vni/mobile-white-paper-c11-520862.html, accessed: 2017-03-22.

[4] M. Uysal and H. Nouri, "Optical wireless communications: an emerging technology," in *International Conference on Transparent Optical Networks (ICTON)*, Graz, 2014, pp. 1–7.

[5] J. Kahn and J. Barry, "Wireless infrared communications," *Proceedings of the IEEE*, vol. 85, no. 2, pp. 265–298, 1997.

[6] M. S. Awan, L. C. Horwath, S. S. Muhammad, E. Leitgeb, F. Nadeem, and M. S. Khan, "Characterization of fog and snow attenuations for free-space optical propagation," *Journal of Communications*, vol. 4, no. 8, pp. 533–545, 2009.

[7] M. Achour, "Simulating atmospheric free-space optical propagation: rainfall attenuation," in *Proceedings in High-Power Lasers and Applications*. International Society for Optics and Photonics, 2002, pp. 192–201.

[8] J. Pan, M. Evans, T. Euler, H. Johnson, and F. DeNap, "Free-space optical communications: opportunities and challenges from a carrier's perspective," in *Proceedings of Asia-Pacific Optical and Wireless Communications*. International Society for Optics and Photonics, 2002, pp. 58–72.

[9] M. Lu, "Raptor-coded free-space optical communication experiment," Master's thesis, McMaster University, 2015.

[10] M. A. Khalighi and M. Uysal, "Survey on free space optical communication: A communication theory perspective," *IEEE Communication Surveys and Tutorials*, vol. 16, no. 4, pp. 2231–2257, 2014.

[11] S. G. Wilson, M. Brandt-Pearce, Q. Cao, and J. H. L. III, "Free-space optical MIMO transmission with Q-ary PPM," *IEEE Transactions on Communications*, vol. 52, no. 6, pp. 2551–2567, 2006.

[12] W. Zhang, S. Hranilovic, and C. Shi, "Soft-switching hybrid FSO/RF links using short-length Raptor codes: design and implementation," *IEEE Journal on selected areas in communications*, vol. 27, no. 9, pp. 1698–1708, 2009.

[13] G. Parca, A. Shahpari, V. Carrozzo, G. T. Beleffi, and A. Teixeira, "Optical wireless transmission at 1.6-Tbit/s (16×100 Gbit/s) for next-generation convergent urban infrastructures," *Optical Engineering*, vol. 52, no. 11, 2013.

[14] Z. Xu, H. Ding, B. M. Sadler, and G. Chen, "Analytical performance study of solar blind non-line-of-sight ultraviolet short-range communication links," *Optics Letters*, vol. 33, no. 16, pp. 1860–1862, 2008.

[15] H. Elgala, R. Mesleh, and H. Haas, "Indoor optical wireless communication: potential and state-of-the-art," *IEEE Communications Magazine*, vol. 49, no. 9, pp. 56–62, 2011.

[16] U.S. Office of Energy Efficiency and Renewable Energy, "LED lighting forecast," https://www.energy.gov/eere/ssl/led-lighting-forecast, accessed: 2017-04-15.

[17] S. Pimputkar, J. S. Speck, S. P. DenBaars, and S. Nakamura, "Prospects for LED lighting," *Nature Photonics*, vol. 3, no. 4, pp. 180–182, 2009.

[18] N. R. Canada, "Canada's standard for efficient light bulbs," http://www.nrcan.gc.ca/energy/regulations-codes-standards/7281, accessed: 2017-03-19.

[19] S. Lim, D. Kang, O. Ogunseitan, and J. Schoenung, "Potential environmental impacts of light-emitting diodes (LEDs): metallic resources, toxicity, and hazardous waste classification," *Environmental Science and Technology*, vol. 45, no. 1, pp. 320–327, 2011.

[20] E. Monteiro, "Design and implementation of color-shift keying for visible light communications," Master's thesis, McMaster University, 2013.

[21] T. Komine and M. Nakagawa, "Fundamental analysis for visible-light communication system using LED lights," *IEEE Transactions on Consumer Electronics*, vol. 50, no. 1, pp. 100–107, 2004.

[22] S. Rajagopal, R. D. Roberts, and S.-K. Lim, "IEEE 802.15.7 visible light communication: modulation schemes and dimming support," *IEEE Communications Magazine*, vol. 50, no. 3, pp. 72–82, 2012.

[23] H. Haas, L. Yin, Y. Wang, and C. Chen, "What is LiFi," *Journal of Lightwave Technology*, vol. 34, no. 6, pp. 1533–1544, 2016.

[24] D. Tsonev, S. Sinanovic, and H. Haas, "Complete modeling of nonlinear distortion in OFDM-based optical wireless communication," *Journal of Lightwave Technology*, vol. 31, no. 18, pp. 3064–3076, 2013.

[25] PureLiFi, "PureLiFi," http://purelifi.com/, accessed: 2017-04-15.

[26] ByteLight, "ByteLight," http://bytelight.com/, accessed: 2017-04-15.

[27] PureLiFi, "LiFi-X: the fastest, smallest and most secure LiFi system," http://purelifi.com/lifi-products/lifi-x/, accessed: 2017-04-15.

[28] J. Grubor, S. Randel, K. D. Langer, F. D. Langer, and J. W. Walewski, "Broadband information broadcasting using LED-based interior lighting," *Journal of Lightwave Technology*, vol. 26, no. 24, pp. 3883–3892, 2008.

[29] W. Chewpraditkul, L. Swiderski, M. Moszynski, T. Szczesniak, A. Syntfeld-Kazuch, C. Wanarak, and P. Limsuwan, "Scintillation properties of LuAG:Ce ,YAG:Ce and LYSO:Ce crystals for Gamma-Ray detection," *IEEE Transaction on Nuclear Science*, vol. 56, no. 6, pp. 3800–3804, 2009.

[30] D. O'Brien, L. Zeng, H. Le-Minh, G. Faulkner, J. Walewski, and S. Randel, "Visible light communications: Challenges and possibilities," in *Proc.*

IEEE 19th International Symposium on Personal, Indoor and Mobile Radio Communications, Cannes, (PIMRC), France, 2008, pp. 1–5.

[31] PureLiFi, "The future of VLC modulation is OFDM," http://purelifi.com/the-future-of-vlc-modulation-ofdm/, accessed: 2017-04-17.

[32] J. Armstrong, "OFDM for optical communication," *Journal of Lightwave*, vol. 27, no. 3, 2009.

[33] M. Z. Afgani, H. Haas, H. Elgala, and D. Knipp, "Visible light communication using OFDM," in *2nd International Conference on Testbeds and Research Infrastructures for the Development of Networks and Communities, TRIDENTCOM*, 2006.

[34] S. D. Dissanayake and J. Armstrong, "Comparison of asymmetrically clipped optical OFDM and DC-biased optical OFDM in AWGN," *IEEE Communications Letters*, vol. 12, no. 5, 2008.

[35] M. S. A. Mossaad, S. Hranilovic, and L. Lampe, "Visible light communications using OFDM and multiple LEDs," *IEEE Transactions on Communications*, vol. 63, no. 11, pp. 4304–4313, 2015.

[36] S. D. Dissanayake, K. Panta, and J. Armstrong, "A novel technique to simultaneously transmit ACO-OFDM and DCO-OFDM in IM/DD systems," in *Proc. IEEE GLOBECOM Workshops*, Houston, TX, USA, 2011, pp. 782–786.

[37] J. Vucic, C. Kottke, S. Nerreter, K. D. Langer, and J. W. Walewski, "513 Mbit/s visible light communications link based on DMT-modulation of a white LED," *Journal of Lightwave Technology*, vol. 28, no. 24, pp. 3512–3518, 2010.

[38] Wikipedia, "MIMO," https://en.wikipedia.org/wiki/MIMO#Standards_and_commercialization, accessed: 2017-03-19.

[39] J. Kahn, W. Krause, and J.B.Carruthers, "Experimental characterization of non-directed indoor infrared channels," *IEEE Transactions on Communications*, vol. 43, no. 234, pp. 1613–1623, 2002.

[40] S. Hranilovic and F. Kschischang, "A pixelated MIMO wireless optical communication system," *IEEE Journal of Selected Topics in Quantum Electronics*, vol. 12, no. 4, pp. 859–874, 2006.

[41] Denso Wave Incorporated, "History of QR code," http://www.qrcode.com/en/history/, accessed: 2016-02-21.

[42] Jolly Technologies Inc, "Data matrix barcode," http://www.jollytech.com/technologies/barcode-symbologies/data-matrix-barcode.php, accessed: 2016-04-15.

[43] L. A. Jr and H. R. M, "Two dimensional data encoding structure and symbology for use with optical readers," US5591956 (A) D 1997-01-07.

[44] A. Mohan, G. Woo, S. Hiura, Q. Smithwick, and R. Raskar, "Bokode: imperceptible visual tags for camera based interaction from a distance," *ACM Transactions on Graphics*, vol. 28, no. 3, pp. 98:1–98:8, 2009.

[45] A. Dabbo, "Theory and design of wireless optical MIMO links," Master's thesis, McMaster University, 2008.

[46] D. Psaltis and G. W. Burr, "Holographic data storage," *Computer*, vol. 31, no. 2, pp. 52–60, 1998.

[47] J. Ashley, M. Bernal, G. W. Burr, H. Coufal, H. Guenther, J. A. Hoffnagle, C. M. Jefferson, B. Marcus, R. M. Macfarlane, R. M. Shelby, and G. T. Sincerbox, "Holographic data storage technology," *IBM Journal of Research and Development*, vol. 44, no. 3, pp. 341–368, 2000.

[48] K. Anderson, E. Fotheringham, A. Hill, B. Sissom, and K. Curtis, "High speed holographic data storage at 500 Gbit/in^2," InPhase Technologies Whitepapers, 2006.

[49] L. Zeng, D. C. O'Brien, H. L. Minh, and G. E. Faulkner, "High data rate multiple input multiple output (MIMO) optical wireless communications using white LED lighting," *IEEE Journal on Selected Areas in Communications*, vol. 27, no. 9, pp. 1654–1662, 2009.

[50] A. H. Azhar, T. A. Tran, and D. O'Brien, "A Gigabit/s indoor wireless transmission using MIMO-OFDM visible-light communications," *IEEE Photonics Technology Letters*, vol. 25, no. 2, pp. 171–174, 2012.

[51] R. Mesleh, H. Elgala, and H. Haas, "Optical spatial modulation," *IEEE/OSA Journal of Optical Communications and Networking*, vol. 3, no. 3, pp. 234 – 244, 2011.

[52] R. Y. Mesleh, H. Haas, S. Sinanovic, C. W. Ahn, and S. Yun, "Spatial modulation," *IEEE Transactions on Vehicular Technology*, vol. 57, no. 4, pp. 2228 – 2241, 2008.

[53] A. Ashok, M. Gruteser, N. Mandayam, and K. Dana, "Characterizing

multiplexing and diversity in visual MIMO," in *45th Annual Conference on Information Sciences and Systems (CISS)*, 2011, pp. 1–6.

[54] A. Ashok, S. Jain, M. Gruteser, N. Mandayam, W. Yuan, and K. Dana, "Capacity of pervasive camera based communications under perspective distortions," in *PerCom: Proceedings of IEEE International Conference on Pervasive Computing and Communications*, Budapest, 2014, pp. 112–120.

[55] M. R. H. Mondal and J. Armstrong, "Analysis of the effect of vignetting on MIMO optical wireless systems using spatial OFDM," *Journal of Lightwave Technology*, vol. 32, no. 5, pp. 922–929, 2014.

[56] A. Motahari and M. Adjouadi, "Barcode modulation method for data transmission in mobile devices," *IEEE Transactions on Multimedia*, vol. 17, no. 1, pp. 118–127, 2015.

[57] T. Hao, R. Zhou, and G. Xing, "COBRA: Color barcode streaming for smartphone systems," in *the Int. Conf. Mobile Systems, Applications and Services*, Lake District, U.K., 2012.

[58] S. D. Perli, N. Ahmed, and D. Katabi, "PixNet: Interference-free wireless links using LCD-camera pairs," in *the Int. Conf. Mobile Computing and Networking*, Chicago, IL, USA, 2010.

[59] A. Ashok, M. Gruteser, N. Mandayam, T. Kwon, W. Yuan, M. Varga, and K. Dana, "Rate adaptation in visual MIMO," in *Proceedings of IEEE Conference on Sensor, Mesh and Ad Hoc Communications and Networks (SECON)*, 2011, pp. 583–591.

[60] B. Han and S. Hranilovic, "A fixed-scale pixelated MIMO visible light communication system," *IEEE JSAC Special Issue on Localisation, Communication and Networking with VLC*, 2017.

[61] M. Luby, A. Shokrollahi, M. Watson, T. Stockhammer, and L. Minder, "Raptor forward error correction scheme for object delivery," Patent, 2007.

[62] J. E. Greivenkamp, *Field Guide to Geometrical Optics*. SPIE Press, 2004.

[63] J. W. Goodman, *Introduction to Fourier Optics*. Roberts and Company Publishers, 2005.

[64] S. Hranilovic, *Wireless Optical Communication Systems*. Springer, 2004.

[65] P. Horowitz and W. Hill, *The Art of Electronics*. Cambridge University Press, 1989.

[66] EMVA, "EMVA standard 1288: Standard for characterization of image sensors and cameras," http://www.emva.org/wp-content/uploads/EMVA1288-3.0.pdf, accessed: 2017-02-22.

[67] Wikipedia, "Fixed pattern noise," https://en.wikipedia.org/wiki/Fixed-pattern_noise, accessed: 2017-02-22.

[68] "Liquid-crystal display," https://en.wikipedia.org/wiki/Liquid-crystal_display, accessed: 2017-03-02.

[69] S. Chandrasekhar, *Liquid Crystals*. Cambridge University Press, 1992.

[70] "Average LCD panel price," http://www.witsview.com/#PanelPrice, accessed: 2017-03-02.

[71] A. Hedge, "Ergonomics considerations of LCD versus CRT displays," pp. 2–3, 2003.

[72] R. Hagberg, "Wall mounting: A solution to LCD/LED TV viewing angle issues," http://www.sanus.com/assets/literature/pdf/wppr_cedia.pdf, accessed: 2017-03-12.

[73] D. Ammermann and W. Kowalsky, "Multilayer organic light emitting diodes for flat panel displays," https://www.tu-braunschweig.de/Medien-DB/ihf/p048-058.pdf, accessed: 2017-03-12.

[74] I. Atik, O. F. Farsakoglu, N. Watsuji, and S. Yilmaz, "Determination of electrical and optical design parameters of high-efficiency OLED," *International Journal of Advanced Research in Computer and Communication Engineering*, vol. 5, no. 5, pp. 949–953, 2016.

[75] B. N. Patel and M. M. Prajapati, "OLED: A modern display technology," *International Journal of Scientific and Research Publications*, vol. 4, no. 6, 2014.

[76] Wikipedia, "OLED," https://en.wikipedia.org/wiki/OLED#Disadvantages, accessed: 2017-03-12.

[77] "More information about LED sizes," http://www.modeltrainsoftware.com/led-sizes-explained.html, accessed: 2017-04-12.

[78] "LED displays: estimating optimal viewing distance and display size," https://www.christiedigital.com/en-us/digital-signage/visual-display-technology/resources/LED-displays, accessed: 2017-03-12.

[79] J. J. D. McKendry, D. Massoubre, S. Zhang, B. R. Rae, R. P. Green, E. Gu, R. K. Henderson, A. E. Kelly, and M. D. Dawson, "Visible-light communications using a CMOS-controlled micro-light-emitting-diode array," *Journal of Lightwave Technology*, vol. 30, no. 1, pp. 61–67, 2012.

[80] X. Li, N. Bamiedakis, J. Wei, J. J. D. McKendry, E. Xie, R. Ferreira, E. Gu, M. D. Dawson, R. V. Penty, and I. H. White, "μLED-based single-wavelength bi-directional POF link with 10 Gb/s aggregate data rate," *Journal of Lightwave Technology*, vol. 33, no. 17, pp. 3571–3576, 2015.

[81] H. Jiang and J. Lin, "Nitride micro-LEDs and beyond - a decade progress review," *Opt. Express=*, pp. 475–484, 2013.

[82] "Comparison between LCD, OLED and μLED," http://technews.tw/2016/09/22/micro-led-ledinside-forum-2016/, accessed: 2017-03-12.

[83] Axis Communications, "CCD and CMOS sensor technology-technical white paper," https://www.axis.com/files/whitepaper/wp_ccd_cmos_40722_en_1010_lo.pdf, accessed: 2017-03-12.

[84] Allied Vision, "CCD or CMOS: can CMOS sensors replace CCDs in all cases," http://www.stemmer-imaging.co.uk/media/uploads/cameras/avt/12/120483-Allied_Vision_White_Paper_CCD_vs_CMOS.pdf, accessed: 2017-03-12.

[85] M. Butler and N. Humphrey, "ROI processing offers opportunities," http://www.vision-systems.com/articles/print/volume-11/issue-5/features/component-integration/roi-processing-offers-opportunities.html, accessed: 2017-04-12.

[86] Edmund Optics, "Optical lenses," https://www.edmundoptics.com/optics/optical-lenses/, accessed: 2017-03-12.

[87] J. Chaves, *Introduction to Nonimaging Optics*. CRC Press, 2015.

[88] R. Kingslake, *Lenses in photography: The practical guide to optics for photographers*. Case-Hoyt Corporation, 1952.

[89] D. J. MacKay, "Fountain codes," *IEEE Proceedings-Communications*, vol. 152, no. 6, pp. 1062–1068, 2005.

[90] M. Luby, "LT codes," in *Proceedings of the 43rd Annual IEEE Symposium on Foundations of Computer Science*, 2002, pp. 271–280.

[91] 3GPP TS 26.346 V6.1.0, "Technical specification group services and system aspects; multimedia broadcast/multicast service; protocols and codecs," Patent, June 2005.

[92] K. Hu, J. Castura, and Y. Mao, "Performance-complexity tradeoffs of Raptor codes over Gaussian channels," *IEEE Communications letters*, vol. 11, no. 4, pp. 343–345, 2007.

[93] B. Sivasubramanian and H. Leib, "Fixed-rate Raptor code performance over correlated Rayleigh fading channels," *Canadian Conference on Electrical and Computer Engineering*, pp. 912–915, 2007.

[94] M. T. Taylor and S. Hranilovic, "Angular diversity approach to indoor positioning using visible light," in *Globecom Workshops (GC Wkshps), 2013 IEEE*, 2013, pp. 1039–1098.

[95] Lenovo, "Thinkvision L192p 19.0-inch monitor-overview," https://support.lenovo.com/ca/en/documents/migr-62656, accessed: 2017-02-2.

[96] Mikrotron GmbH, "Mc13xx users manual," 2003.

[97] Edmundoptics, "Double convex lens," https://www.edmundoptics.com/optics/optical-lenses/double-convex-dcx-spherical-singlet-lenses/uncoated-double-convex-dcx-lenses/32-978/, accessed: 2017-02-2.

[98] J. Canny, "A computational approach to edge detection," *IEEE Transactions on Pattern Analysis and Machine Intellegence*, vol. PAMI-8, no. 6, pp. 679–698, 1986.

[99] R. Duda and P. Hart, *Pattern Classification and Scene Analysis*. John Wiley and Sons, 1973.

[100] G. Ungerboeck, "Channel coding with multilevel/phase signals," *IEEE Transactions on Information Theory*, vol. 28, no. 1, pp. 55–67, 1982.